The dual effect of ephaptic coupling on cardiac conduction with heterogeneous expression of connexin 43

Ning Wei[a], Yoichiro Mori[a], Elena G. Tolkacheva[b,*]

[a]*School of Mathematics, University of Minnesota, Minneapolis, MN 55455*
[b]*Department of Biomedical Engineering, University of Minnesota, Minneapolis, MN 55455*

Abstract

Decreased and heterogeneous expression of connexin 43 (Cx43) are common features in animal heart failure models. Ephpatic coupling, which relies on the presence of junctional cleft space between the ends of adjacent cells, has been suggested to play a more active role in mediating intercellular electrical communication when gap junctions are reduced. To better understand the interplay of Cx43 expression and ephaptic coupling on cardiac conduction during heart failure, we performed numerical simulations on our model when Cx43 expression is reduced and heterogeneous. Under severely reduced Cx43 expression, we identified three new phenomena in the presence of ephaptic coupling: alternating conduction, in which ephaptic and gap junction-mediated mechanisms alternate; instability of planar fronts; and small amplitude action potential (SAP), which has a smaller potential amplitude than the normal action potential. In the presence of heterogeneous Cx43 expression, ephaptic coupling can either prevent or promote con-

*Corresponding author
Email address: talkacal@umn.edu (Elena G. Tolkacheva)
[1]Address: 312 Church St. SE, 6-128 Nils Hasselmo Hall, Minneapolis, MN 55455.
[2]Tel.: +1612 626 2719.

duction block (CB) depending on the Cx43 knockout (Cx43KO) content. When Cx43KO content is relatively high, ephaptic coupling reduces the probabilities of CB. However, ephaptic coupling promotes CB when Cx43KO and wild type cells are mixed in roughly equal proportion, which can be attributed to an increase in current-to-load mismatch.

Keywords: Heterogeneous connexin 43, Bidomain model, Alternating conduction, Small amplitude action potential, Instability of planar fronts, Conduction block.

---

1. Introduction

Cardiac cells communicate electrically to coordinate the muscular contraction of the heart to pump blood. Gap junctions are low-resistance pathways that mediate the electrical impulses between myocytes. Gap junctional coupling is one of the key factors that guarantees the velocity and reliability of cardiac conduction Shaw and Rudy (1997); Vaidya et al. (2001); Beauchamp et al. (2004, 2012).

Ventricular myocytes are connected electrically through gap junction channels formed mainly by connexin 43 (Cx43) and, to a smaller extent, Cx45 Davis et al. (1995). Growing experimental and theoretical evidence suggests that heterogeneity of Cx43 can lead to altered patterns of conduction, re-entrant arrhythmias and sudden death, Danik et al. (2004); Gutstein et al. (2001); Jongsma and Wilders (2000); Kanno and Saffitz (2001); Prudat and Kucera (2014). For example, in Danik et al. (2004), authors investigated susceptibility to arrhythmias in a genetically engineered murine model to express progressively decreasing levels of Cx43. Lethal tachyarrhythmias were initiated if cardiac Cx43 abundance was decreased in a heterogeneous fashion to 18% of the control level. In Gutstein et al.

(2001), authors designed a murine model of heterogeneous gap junction channel expression, which results in conduction defects as well as markedly depressed contractile function. Additionally, in Prudat and Kucera (2014), authors showed that velocity and stability of conduction behave in a nonlinear manner when cardiomyocytes expressing different amounts of Cx43 are combined. In particular, conduction became very heterogeneous and was susceptible to block in the coculturing of Cx43 knockout (Cx43KO) and wild type (WT) cells, while block was never observed in monogenotypic preparations.

It is widely accepted that gap junctional coupling is the primary mechanism responsible for electrical communication between cardiac cells Rohr (2004). However, recent experimental observation has raised the question of whether conduction can be sustained in the absence of gap junctions Danik et al. (2004); Yao et al. (2003). For instance, in Yao et al. (2003), intercellular conductance measured by dual whole cell voltage clamp in pairs of adult rat ventricular myocytes with genetic Cx43 ablation was dramatically reduced from 588 nS to 10 nS. However, impulse propagation was reduced by only 50% in tissue composed of the same cells.

One possible explanation of this intriguing observation is ephaptic coupling, first proposed in Sperelakis and Mann (1977) and futher elaborated in Sperelakis and McConnell (2002). In it, neighboring cells are electrically coupled through a narrow cleft space that is resistively connected to the extracellular space. It is further assumed that Na^+ channels are preferentially localized to the cleft space, as shown by experiments in Cohen (1996); Maier et al. (2002); Kucera et al. (2002); Sperelakis and McConnell (2002). When an action potential reaches one cell, the Na^+ current flows into the cell from extracellular bath via the cleft, and the

potential in the cleft space drops. Once the cleft potential becomes sufficiently negative, it depolarizes the membrane of the adjacent cell to the threshold, and that cell then produces an action potential. Several theoretical studies investigated the possible role of ephaptic coupling in cardiac signal propagation Kucera et al. (2002); Mori et al. (2008); Veeraraghavan et al. (2014b); Hand and Peskin (2010); Copene and Keener (2008). In Kucera et al. (2002); Hand and Peskin (2010), the authors assessed the hypothesis that conduction could be modulated by the preferential localization of Na^+ channels in the cleft space, which causes a large negative potential in the cleft and influences conduction in two opposite ways, depending on the strength of gap junctional coupling. In particular, for normal and moderately reduced gap junctional coupling, localization of Na^+ channels to the cleft space forces Na^+ current to go through the large resistance between cleft and extracellular space, which slowed down the conduction. In contrast, for greatly reduced gap junctional coupling, the negative cleft potential induced by Na^+ current in the prejunctional membrane lead to a suprathreshold depolarization of the postjunctional membrane, which facilitated and accelerated conduction. In Mori et al. (2008), the authors identified a mode of conduction in which the ephaptic and gap-junction-mediated mechanisms alternate. Authors of Copene and Keener (2008) explored the feasibility of ephaptic mechanism in the absence of gap junctions, which is highly parameter dependent.

Decreased and heterogeneous expression of Cx43 are common features in animal heart failure models Wang and Gerdes (1999); HUANG et al. (1999); Yoshida et al. (2011). Emerging evidence suggests a more active role for ephaptic coupling in mediating intercellular electrical communication when gap junctions are reduced in a homogeneous maner Yao et al. (2003); Kucera et al. (2002); Hand

and Peskin (2010); Lin and Keener (2014). However, the interplay between heterogeneous Cx43 expression and ephaptic coupling on cardiac conduction has not been investigated yet. In this manuscript, we aim to explore the effects of ephaptic coupling on cardiac impulse propagation via numerical simulations when Cx43 expression is reduced and heterogeneous.

2. Materials and Methods

2.1. Mathematical model

2.1.1. Bidomain model with ephaptic coupling

A two dimensional (2D) bidomain model (Fig. 1A) of electrical conduction was modified to incorporate ephaptic coupling Hand and Peskin (2010); Copene and Keener (2008), which relies on the presence of a junctional cleft space between the ends of adjacent cells. Each cell is assumed to be cylindrical in shape with radius r and length L. The cells are connected by gap junctions to form an $M \times N$ rectangular lattice. At each lattice point (i, j), we associated intracellular potential $\phi_i^{(i,j)}$ and extracellular potential $\phi_e^{(i,j)}$. The cleft lies in between cells (i, j) and $(i, j+1)$. We then defined a cleft potential $\phi_c^{(i,j+\frac{1}{2})}$ at location $(i, j+\frac{1}{2})$. We called the space, which lies in the extracellular space and stays adjacent to the cleft, the extracellular-cleft space. The potential in the extracellular-cleft space is denoted by $\phi_{ec}^{(i,j+\frac{1}{2})}$. Note that Fig. 1A shows the lattice view of the model, whereas Fig. 1B shows the connection between lattices. In particular, Fig. 1B shows a circuit diagram for two adjacent cells that are ephaptically coupled through a common cleft space in the presence of end-to-end gap junctions (GJ_{end}), side-to-side gap junctions (GJ_{side}) and resistive connections between extracellular spaces (R_{ee}) are not shown here. Cleft space was modelled as a single narrow

compartment with resistive connections (R_c) to the extracellular space; Resistive connections between extracellular space and the extracellular-cleft space are denoted by R_{ec}. Intracellular and extracellular spaces of each cell are separated by the cell side membrane; intracellular and cleft spaces are separated by the cell end membrane. Both side and end membranes allow the free flow of ionic and capacitive currents. Ephaptic coupling is maintained by the active end membranes that are connected by a shared cleft potential. In order to save on computational cost, we treated intracellular and extracellular spaces of each cell to be isopotential.

As can be seen from Fig. 1, four different compartments, namely intracellular, extracellular, cleft, and extracellular-cleft spaces, were modelled separately. Current conservation in each compartment provides the following equations, with parameters listed in Table 1.

- Intracellular space ($\phi_i^{(i,j)}$; $1 \leqslant i \leqslant M$, $2 \leqslant j \leqslant N-1$) :

$$\begin{aligned} &GJ_{\text{end}}(\phi_i^{(i,j)} - \phi_i^{(i,j-1)}) + GJ_{\text{end}}(\phi_i^{(i,j)} - \phi_i^{(i,j+1)}) \\ &+GJ_{\text{side}}(\phi_i^{(i,j)} - \phi_i^{(i-1,j)}) + GJ_{\text{side}}(\phi_i^{(i,j)} - \phi_i^{(i+1,j)}) \\ &+A_{\text{end}}C_m\frac{\partial(\phi_i^{(i,j)} - \phi_c^{(i,j-\frac{1}{2})})}{\partial t} + A_{\text{end}}C_m\frac{\partial(\phi_i^{(i,j)} - \phi_c^{(i,j+\frac{1}{2})})}{\partial t} + I_{\text{end}} \\ &+A_{\text{side}}C_m\frac{\partial(\phi_i^{(i,j)} - \phi_e^{(i,j)})}{\partial t} + I_{\text{side}} = 0, \end{aligned} \tag{2.1}$$

where $A_{\text{end}} = \pi r^2$ and $A_{\text{side}} = 2\pi rL$ denote the cross-sectional and side areas of a cell, respectively; $GJ_{\text{end}} = A_{\text{end}}g_{\text{end}}$ and $GJ_{\text{side}} = \frac{A_{\text{side}}}{2}g_{\text{side}}$ denote end-to-end and side-to-side gap junctional conductance, respectively; $\phi_i^{(i,j)}$, $\phi_i^{(i,j-1)}$ and $\phi_i^{(i,j+1)}$ denote the intracellular potentials of cells (i,j), $(i,j-1)$ and $(i,j+1)$, respectively; $\phi_i^{(i-1,j)}$ and $\phi_i^{(i+1,j)}$ denote the intracellular potentials of cells $(i-1,j)$ and $(i+1,j)$, respectively; $\phi_c^{(i,j-\frac{1}{2})}$ and

$\phi_c^{(i,j+\frac{1}{2})}$ denote cleft potentials at locations $(i, j-\frac{1}{2})$ and $(i, j+\frac{1}{2})$, respectively; C_m represents the membrane capacitance per area; I_{end} and I_{side} denote the outward ionic current of the end and side membranes, respectively; $\phi_e^{(i,j)}$ represents the extracellular potential of cell (i, j).

Note that for $j = 1$, terms $GJ_{\text{end}}(\phi_i^{(i,j)} - \phi_i^{(i,j-1)})$ and $A_{\text{end}}C_m\frac{\partial(\phi_i^{(i,j)}-\phi_c^{(i,j-\frac{1}{2})})}{\partial t}$ are dropped from Eq. (2.1). Similarly, for $j = N$, terms $GJ_{\text{end}}(\phi_i^{(i,j)} - \phi_i^{(i,j+1)})$ and $A_{\text{end}}C_m\frac{\partial(\phi_i^{(i,j)}-\phi_c^{(i,j+\frac{1}{2})})}{\partial t}$ are dropped from Eq. (2.1). In order to minimize the edge effects, we imposed periodic boundary condition in the x direction (see Fig. 1A): we identified $\phi_i^{(i-1,j)}$ with $\phi_i^{(M,j)}$ for $i = 1$, and we identified $\phi_i^{(i+1,j)}$ with $\phi_i^{(1,j)}$ for $i = M$.

- Extracellular space ($\phi_e^{(i,j)}$; $1 \leqslant i \leqslant M$, $2 \leqslant j \leqslant N-1$) :

$$\begin{aligned} &\frac{\phi_e^{(i,j)} - \phi_{ec}^{(i,j-\frac{1}{2})}}{R_{ec}} + \frac{\phi_e^{(i,j)} - \phi_{ec}^{(i,j+\frac{1}{2})}}{R_{ec}} \\ &+\frac{\phi_e^{(i,j)} - \phi_e^{(i-1,j)}}{R_{ee}} + \frac{\phi_e^{(i,j)} - \phi_e^{(i+1,j)}}{R_{ee}} \\ &-A_{\text{side}}C_m\frac{\partial(\phi_i^{(i,j)} - \phi_e^{(i,j)})}{\partial t} - I_{\text{side}} = 0, \end{aligned} \tag{2.2}$$

where $\phi_{ec}^{(i,j-\frac{1}{2})}$ and $\phi_{ec}^{(i,j+\frac{1}{2})}$ denotes the extracellular-cleft potentials at location $(i, j-\frac{1}{2})$ and $(i, j+\frac{1}{2})$, respectively; R_{ec} represents the resistance between extracellular space and the extracellular-cleft space; $\phi_e^{(i-1,j)}$ and $\phi_e^{(i+1,j)}$ denote the extracellular potentials of cells $(i-1, j)$ and $(i+1, j)$, respectively; R_{ee} represents the resistance between extracellular spaces in the x direction (see Fig. 1A).

Note that for $j = 1$, term $\frac{\phi_e^{(i,j)}-\phi_{ec}^{(i,j-\frac{1}{2})}}{R_{ec}}$ is dropped from Eq. (2.2). Similarly, for $j = N$, $\frac{\phi_e^{(i,j)}-\phi_{ec}^{(i,j+\frac{1}{2})}}{R_{ec}}$ is dropped from Eq. (2.2). In order to minimize

the edge effects, we imposed periodic boundary condition in the x direction (see Fig. 1A): we identified $\phi_e^{(i-1,j)}$ with $\phi_e^{(M,j)}$ for $i = 1$, and we identified $\phi_e^{(i+1,j)}$ with $\phi_e^{(1,j)}$ for $i = M$.

- Cleft space ($\phi_c^{(i,j+\frac{1}{2})}$; $1 \leqslant i \leqslant M$, $1 \leqslant j \leqslant N-1$):

$$-A_{\text{end}}C_m\frac{\partial(\phi_i^{(i,j)}-\phi_{\text{c}}^{(i,j+\frac{1}{2})})}{\partial t}-A_{\text{end}}C_m\frac{\partial(\phi_i^{(i,j+1)}-\phi_{\text{c}}^{(i,j+\frac{1}{2})})}{\partial t}-I_{\text{end}} + \frac{\phi_c^{(i,j+\frac{1}{2})}-\phi_{ec}^{(i,j+\frac{1}{2})}}{R_c}=0, \tag{2.3}$$

where R_c represents the resistance between cleft and extracellular space.

- Extracellular-cleft space ($\phi_{ec}^{(i,j+\frac{1}{2})}$; $1 \leqslant i \leqslant M$, $1 \leqslant j \leqslant N-1$):

$$-\frac{\phi_e^{(i,j)}-\phi_{ec}^{(i,j+\frac{1}{2})}}{R_{ec}}-\frac{\phi_e^{(i,j+1)}-\phi_{ec}^{(i,j+\frac{1}{2})}}{R_{ec}}-\frac{\phi_c^{(i,j+\frac{1}{2})}-\phi_{ec}^{(i,j+\frac{1}{2})}}{R_c}=0. \tag{2.4}$$

2.1.2. Modeling Cx43 expression

Since we aim to study the effect of distribution pattern of Cx43KO and WT cells on conduction features in the presence of ephaptic coupling, we followed Prudat and Kucera (2014) to model heterogeneous Cx43 expression, where genotypes of cells were allocated stochastically according to the predefined Cx43KO content (p). In other words, under each p, we stochastically assigned cell genotypes to be Cx43KO or WT. Here, $p = 0$ implies that the Cx43KO content is 0%, i.e. all cells are WT. In contrast, $p = 1$ implies that Cx43KO content is 100%, i.e. all cells are knockout.

Conductance of gap junctions was set proportionally to the area of contacts between adjacent cells using proportionality constants g_{end} and g_{side} (Table 1) for end-to-end and side-to-side contacts, respectively. For connections between

WT cells, g_{end} and g_{side} were scaled by a factor k_{WT} (Table 1). For connections between Cx43KO cells, g_{end} and g_{side} were scaled by a factor k_{Cx43KO} (Table 1). The value of k_{Cx43KO} (Table 1) was chosen to keep the longitudinal conduction velocity (CV_L) in the absence of ephaptic coupling (which can be modelled by a sufficiently large cleft width) the same as CV_L for Cx43KO strands reported in Prudat and Kucera (2014), where ephaptic coupling was not considered.

As reported in previous studies, the residual low connexin expressions between Cx43KO and WT cells are mediated by Cx43/Cx45 Beauchamp et al. (2012); McCain et al. (2012). For connections between WT and Cx43KO cells, g_{end} and g_{side} were also scaled by the factor k_{Cx43KO} based on the assumption that the coupling between cells is essentially determined by the cell expressing the least amount of connexins Beauchamp et al. (2012). In Beauchamp et al. (2012), the authors experimentally measures the intercellular conductance between pairs of ventricular myocytes with different Cx43 expression. They found that ablation of Cx43 in one cell of a pair caused a marked decrease in mean intercellular conductance, from 68.3$\pm$9.6 nS to 5.2$\pm$1.7 nS.

2.1.3. Membrane currents

The excitable dynamics of normal cardiac tissue was described by Luo-Rudy dynamic guinea pig ventricular model 2007 (LRd 2007) Livshitz and Rudy (2007). Two different distributions were used for Na^+ channels: (1) uniform distribution, in which Na^+ channels are evenly distributed along the cell membrane; (2) localized distribution, in which all Na^+ channels are localized to the cleft spaces at the two cell ends, while the total conductance of Na^+ channels is fixed to its normal value. In this study, Na^+ channels are assumed to be localized to the cleft, unless indicated otherwise. The other ionic channels of LRd 2007 model are uniformly

distributed along the cell membrane.

Table 1: Parameters that enter our model

Symbol	Parameter	Value/Expression	Reference
r	Radius of cell	1.1×10^{-3} cm	Hand and Peskin (2010)
L	Length of cell	10^{-2} cm	Hand and Peskin (2010)
g_{end}	End-to-end gap junctional conductance per area	6.66×10^2 mS/cm^2	Hand and Peskin (2010)
α	Ratio between g_{end} and g_{side}	6	Hand et al. (2009)
g_{side}	Side-to-side gap junctional conductance per area	$\frac{g_{\text{end}}}{\alpha}$	Derived
C_m	Membrane capacitance per area	1 μF/cm^2	Hand and Peskin (2010)
d_{cleft}	Cleft width	2 – 115 nm	Hand and Peskin (2010)
σ_{ext}	Extracellular conductivity	6.67 mS/cm	Hand and Peskin (2010)
R_c	Resistance between cleft and extracellular space	$\frac{1}{8\pi\sigma_{\text{ext}}d_{\text{cleft}}}$	Hand and Peskin (2010)
AR_x	Anisotropy ratio of resistance in x direction	1.33	Keener and Sneyd (2010)
AR_y	Anisotropy ratio of resistance in y direction	0.35	Keener and Sneyd (2010)
R_{ec}	Resistance between extracellular space and extracellular cleft	$\frac{1}{2\text{AR}_y A_{\text{end}} g_{\text{end}}}$	Keener and Sneyd (2010)
R_{ee}	Resistance between extracellular spaces in x direction	$\frac{2}{\text{AR}_x A_{\text{side}} g_{\text{side}}}$	Keener and Sneyd (2010)
k_{WT}	Scaling factor for g_{end} and g_{side} between WT cells	1	Prudat and Kucera (2014)
k_{Cx43KO}	Scaling factor for g_{end} and g_{side} between Cx43KO cells / WT and Cx43KO cells	0.005	Derived
ϕ_i	Intracellular potential		
ϕ_e	Extracellular potential		
ϕ_c	Cleft potential		
ϕ	Side transmembrane potential	$\phi_i - \phi_e$	

173 *2.2. Numerical simulation*

174 Simulations were run in a lattice consisting of $M \times N$ cells (Fig. 1A), where
175 $M = 2,\ 3,\ 6,\ 10$, and 16, and $N = 75$. Initially, all potentials and gating variables
176 were held at resting states. Conduction was initiated by applying 0.5 ms excitatory
177 current pulses of amplitude 0.15 μA into all cells at the left hand side of the lattice.

178 The resulting model consists of a large number of differential algebraic equa-
179 tions. We used a splitting method by updating the potential and gating variables of
180 ion channels separately to solve the system. When updating the potential, gating
181 variables are fixed; the linear parts of the system (linear in potential) were treated
182 using backward Euler method; the ionic currents and dynamics were linearized
183 and treated using backward Euler method afterwards. The system was solved via
184 a direct method (backslash operator in Matlab).

185 We defined the wavefront of a normal travelling action potential as the spatial
186 location where the side transmembrane potential (ϕ) crosses -30 mV with $\frac{\partial \phi}{\partial t} > 0$.
187 This value was set to distinguish small amplitude action potential (SAP) (Sec.
188 3.2.3) from normal action potential, since SAP does not reach -30 mV. Activation
189 was monitored by identifying the earliest activation time (EAT) at every column
190 of the $M \times N$ lattice (Fig. 1A). $\mathrm{CV_L}$ was computed by linear regression of EAT
191 over 20% to 80% of lattice length to exclude the boundary effect. Conduction
192 block (CB) was defined as the failure of wavefront to reach the right hand side of
193 the lattice.

3. Results

3.1. The effect of ephaptic coupling on cardiac conduction.

To explore the effects of ephaptic coupling on impulse propagation, we identified several possible values of cleft width (d_{cleft}), from 2 nm to 115 nm (see Table 1). Note that smaller d_{cleft} corresponds to larger R_c, which therefore implies stronger ephaptic coupling.

In Figs. 2A and 2B, CV_L is plotted as a function of d_{cleft} for $p = 1$ (A, Cx43KO cells) and $p = 0$ (B, WT cells), respectively. As observed, Fig. 2A displays a biphasic behavior of CV_L: with increasing d_{cleft}, CV_L exhibits a marked increase to 13.1 cm/s (at $d_{\text{cleft}} = 8$ nm) followed by a decrease to 2.5 cm/s with further cleft widening. In contrast, when gap junctional coupling is strong, CV_L shows a monotone increase as d_{cleft} increases (see Fig. 2B). Note that in Fig. 2, the most notable differences in qualitative behaviors of CV_L are seen for $d_{\text{cleft}} < 20$ nm.

To further investigate the effects of ephatic coupling on conduction, we chose $d_{\text{cleft}} = 2$ nm, 3.5 nm, 8 nm, 8.5 nm, and 115 nm as the representative values in our numerical simulations.

3.2. Conduction features when Cx43KO content is 100% ($p = 1$).

To further explore spatiotemporal excitation patterns that occur in the near absence of gap junctions, we performed numerical simulations in lattices consisting of 100% Cx43KO cells. The following three novel conduction features were observed in the presence of ephaptic coupling: alternating conduction (Sec. 3.2.1), instability of planar fronts (Sec. 3.2.2) and SAP (Sec. 3.2.3). However, when gap junction-mediated mechanism dominates (d_{cleft} is sufficiently large), none of these features can be observed. Note that alternating conduction and SAP are one-

dimensional phenomena, which do not depend on lattice width. In contrast, the instability of planar fronts can only be observed in a 2D simulation.

3.2.1. Alternating conduction

Fig. 3 shows EAT as a function of N for $d_{\text{cleft}} = 8.5$ nm (A), 8.6 nm (B), 8.7 nm (C), 8.9 nm (D), which demonstrates the presence of periodic transitions between fast and slow conduction under severely reduced gap junctions. For instance, at $d_{\text{cleft}} = 8.9$ nm, action potential propagates fast between columns N and $N+1$ when N is even, but slowly between columns N and $N+1$ when N is odd. Note that for 9 nm $\leqslant d_{\text{cleft}} \leqslant$ 9.6 nm, the EAT pattern is the same as that for $d_{\text{cleft}} =$ 8.9 nm.

Fig. 4 shows the end transmembrane potential ($\phi_{ic} = \phi_i - \phi_c$) traces of the left ($\phi_{ic\text{L}}$) and right sides ($\phi_{ic\text{R}}$) of cells at location $(3,\, 24)$, $(3,\, 25)$, $(3,\, 26)$ and $(3,\, 27)$, where $d_{\text{cleft}} = 5$ nm (A), 8.9 nm (B) and 10 nm (C). As indicated in Fig. 4B, ϕ_{ic} traces of the fast conduction phase (cell (3, 24) to cell (3, 25), and cell (3, 26) to cell (3, 27) in Fig. 3D) are similar to the potential traces ($\phi_{ic\text{R}}^{(3,\,24)}$, $\phi_{ic\text{L}}^{(3,\,25)}$, $\phi_{ic\text{R}}^{(3,\,26)}$ and $\phi_{ic\text{L}}^{(3,\,27)}$) seen when $d_{\text{cleft}} = 5$ nm, at which the propagation is driven primarily by ephaptic coupling. However, ϕ_{ic} profiles of the slow conduction phase (cell (3, 25) to cell (3, 26) in Fig. 3D) are similar to the potential traces ($\phi_{ic\text{R}}^{(3,\,25)}$ and $\phi_{ic\text{L}}^{(3,\,26)}$) seen when $d_{\text{cleft}} = 10$ nm, at which the conduction can be attributed to the residual gap junctional coupling. Alternating conduction shown in Fig. 3 thus lies in an intermediate regime, in which the two aforementioned mechanisms play an equal role, but spatially alternate in being the dominant mode of conduction. Alternating conduction was reported in Mori et al. (2008), where the authors only demonstrated the pattern similar to the one shown in Fig. 3D. However, patterns seen in Figs. 3A - 3C have never been reported previously.

Note that two upstrokes are observed in $\phi_{ic\mathrm{R}}^{(3,\,25)}$ and $\phi_{ic\mathrm{L}}^{(3,\,26)}$ traces of Fig. 4B and in multiple traces of Fig. 4C. For $\phi_{ic\mathrm{R}}^{(3,\,25)}$ trace in Fig. 4B, the first upstroke corresponds to the depolarization of the right end membrane of cell $(3,\,25)$, which results in a drop in the cleft potential shared by cells $(3,\,25)$ and $(3,\,26)$. The drop in the aforementioned cleft potential gives rise to a passive increase in $\phi_{ic\mathrm{L}}^{(3,\,26)}$ (first upstroke in $\phi_{ic\mathrm{L}}(26)$ trace), which is not large enough to activate the left end membrane of cell (3, 26). Similarly, the depolarization of left end membrane of cell $(3,\,26)$ (second upstroke in $\phi_{ic\mathrm{L}}^{(3,\,26)}$ trace) can lead to a passive increase in $\phi_{ic\mathrm{R}}^{(3,\,25)}$ (second upstroke in $\phi_{ic\mathrm{R}}^{(3,\,25)}$ trace). Similar explanation can be applied to traces in Fig. 4C. However, in Fig. 4A ($d_{\mathrm{cleft}} = 5$ nm), cells are more tightly connected, which gives rise to stronger ephaptic coupling, and therefore, only one upstroke is seen on ϕ_{ic} traces.

We point out that the differences in upstroke timing in the ϕ_{ic} traces of Fig. 4 are primarily a result of ephaptic coupling (for example $\phi_{ic\mathrm{R}}^{(3,\,24)}$ and $\phi_{ic\mathrm{L}}^{(3,\,25)}$ traces) and different action potential arrival times in the cleft spaces (for example $\phi_{ic\mathrm{L}}^{(3,\,25)}$ and $\phi_{ic\mathrm{R}}^{(3,\,25)}$ traces) . The upstroke timing differences here should thus not be confused with the junctional and intracellular delays discussed in Rohr et al. (1998); Shaw and Rudy (1997), where ephaptic coupling were not considered.

3.2.2. Instability of planar fronts

Fig. 5 shows a propagation of an unusual action potential at $d_{\mathrm{cleft}} = 9.8$ nm, in which instability of planar fronts occurs. This effect is only observed for $9.7\text{ nm} \leqslant d_{\mathrm{cleft}} \leqslant 9.8\text{ nm}$. Figs. 5A - 5D show a sequence of snapshots demonstrating propagation when an external current activates all cells at the left hand side of the lattice. The snapshots plot ϕ at time $(t) = 89$ ms (A), 112 ms (B), 139 ms (C) and 173 ms (D). In order to make the wavefront easier to observe, we

rotated the figures by 180°. As indicated in Fig. 5, there is an irregular change in the shape of the wavefront (denoted by black arrows), which proceeds in a zigzag fashion. Such wavefronts propagate to neighboring cells in a spatially heterogeneous manner, rather than evenly along the lattice.

This zigzag wavefront pattern is a result of instability of the planar fronts, reminiscent of stability of front solutions studies in Mori and Matano (2015). Inevitable numerical deviations from the planar front, which will decay and remain small in case of a stable planar front, and grows when the planar front is unstable. Such numerical deviations, in biophysical terms, correspond to external noise; the planar front thus destabilizes in the presence of noise.

We speculate that the instability also results from the presence of two modes of conduction, the ephaptic and the gap junction mediated. Unlike alternating conduction (Sec. 3.2.1) in which the mode of conduction depends only on the y-coordinate (Fig. 1A), here, the mode of conduction depends on the x-direction as well. A checkerboard pattern of ephaptic and gap junction mediated alternation gives rise to the instability of planar fronts.

3.2.3. Small amplitude action potentials (SAP)

Fig. 6 demonstrates a novel type of action potential propagation at $d_{\text{cleft}} = 3.5$ nm, which has a much lower potential amplitude than the normal conduction, with the maximum value of $\phi = -40$ mV. Figs. 6A - 6D show a sequence of snapshots demonstrating SAP when an external current activates all cells at the left hand side of the lattice. The snapshots illustrate ϕ at time (t) = 13 ms (A), 51 ms (B), 80 ms (C) and 126 ms (D), respectively.

Note that propagation patterns depend highly on the values of d_{cleft}. For instance, SAP occurs for 3.5 nm $\leqslant d_{\text{cleft}} \leqslant$ 3.7 nm, while CB occurs for 3.2 nm $\leqslant$

$d_{\text{cleft}} \leqslant 3.4$ nm. For 3.8 nm $\leqslant d_{\text{cleft}} \leqslant 5$ nm, one observes a wave that has characteristics in between normal conduction and SAP (see Fig. 7), reminiscent of stacked fronts observed in Iida et al. (2011). Finally, for 2 nm $\leqslant d_{\text{cleft}} \leqslant 3.1$ nm and $d_{\text{cleft}} > 5$ nm, normal conduction is seen. However, when 2 nm $\leqslant d_{\text{cleft}} \leqslant 3.1$ nm, conduction is extremely slow with $\text{CV}_{\text{L}} = 0.7$ cm/s.

At $d_{\text{cleft}} = 3.5$ nm, R_c is very high. In this case, the cleft potential drops low enough to excite the end membrane. However, the resulting inward Na^+ current is not sufficient to fully activate the side membrane, and therefore SAP occurs. In other words, when SAP occurs, Na^+ channels residing on the end membrane are fully activated, as indicated by the activation gating variable (m_{end}) of Na^+ channels that resides on the end membrane of cell (3, 25) (Fig. 8A). Nevertheless, the side membrane is not fully excited, as indicated by ϕ profile of that cell (Fig. 8B). SAP may thus be seen as a cardiac propagation jumping from cleft to cleft.

When SAP occurs, L-type Ca^{2+} channels are not fully activated. Figs. 9A and 9B show the activation gating variable (d) of Ca^{2+} channels that reside on the end (d_{end}, A) and side (d_{side}, B) membranes of cell (3, 25); Fig. 9C exhibits ϕ profile of cell (3, 25), where $d_{\text{cleft}} = 3.5$ nm (blue), 3.8 nm (red), and 115 nm (green). As observed in Figs. 9A and 9B, gating variable d is not active when SAP occurs ($d_{\text{cleft}} = 3.5$ nm). This is in contrast to normal conduction ($d_{\text{cleft}} = 115$ nm), in which Ca^{2+} channels are fully activated. SAP is thus a wave in which an electrical pulse propagates without a large rise in Ca^{2+} concentration. We may therefore regard SAP as an electromechanically dissociated wave.

As shown in Fig. 9, for $d_{\text{cleft}} = 3.8$ nm, the behaviors of d_{end}, d_{side} and ϕ lie in an intermediate regime. Unlike SAP, the resulting influx of Na^+ current is sufficient to activate Ca^{2+} channels residing on the side membrane, indicated by

d_{side} in Fig. 9B. In other words, the steep depolarization of side membrane results from Na^+ current, whereas the shallow depolarization results from L-type Ca^{2+} current (Fig. 9C). An intermediate wave thus occurs.

3.3. Conduction block (CB) in mixed genotype lattices.

In this section, we aim to investigate the possible impacts of interplay between heterogeneous Cx43 expression and ephaptic coupling on cardiac propagation, specially looking at the occurrence of CB. We performed numerical simulations in an $M \times N$ lattice with a random distribution of WT and Cx43 cells according to the predefined Cx43KO content ($0 \leqslant p \leqslant 1$), while incorporating different values of d_{cleft}. As stated in Sec. 2.2, $M = 2, 3, 6, 10$ and 16, $N = 75$.

For each lattice, numerical simulations were implemented 100 iterations for every p, d_{cleft} and Na^+ channel distribution, thus taking into account different realizations of cellular architecture.

3.3.1. Ephaptic coupling can suppress CB when $p \geqslant 0.7$.

Tables 2 and 3 show the number of CB observed for different p and d_{cleft} in 2×75 and 3×75 lattices, respectively. Note that there is no CB for monogenotypic preparations ($p = 0$ or 1). However, co-culturing of Cx43KO and WT cells results in increased probabilities of CB, especially for $0.2 \leqslant p \leqslant 0.6$. This is consistent with the results of Prudat and Kucera (2014), where CB was studied without ephaptic coupling (corresponding to $d_{\text{cleft}} = 115$ nm in our simulations). Tables 2 and 3 indicate that the proportion of CB in the above range is independent of the value of d_{cleft} and thus of ephaptic coupling.

The number of CB in Tables 2 and 3, however, shows a dependency on d_{cleft} when $0.7 \leqslant p \leqslant 0.9$. The proportion of CB for $d_{\text{cleft}} = 8$ nm is lower than that for

$d_{\text{cleft}} = 115$ nm. Indeed, in Table 2, for $0.7 \leqslant p \leqslant 0.8$, the differences in the number of CB at $d_{\text{cleft}} = 8$ nm and $d_{\text{cleft}} = 115$ nm are statistically significant according to two-proportion z-test ($z = 3.6$ and 2.5, respectively). For $p = 0.9$, statistically significant difference ($z = 2.3$) can be detected if more than 800 numerical experiments are performed (data is not shown in Table 2). In Table 3, for $p = 0.7$, we observed statistically significant difference ($z = 3.3$) in the occurrence of CB between $d_{\text{cleft}} = 8$ nm and 115 nm. At $p = 0.8$, statistically significant difference ($z = 4.8$) can be observed when the number of numerical experiments is increased to 400 (data is not shown in Table 3). Recall that the maximum CV_L was achieved at $d_{\text{cleft}} = 8$ nm (see Fig. 2A) in the near absence of gap junctional coupling; and at $d_{\text{cleft}} = 115$ nm, propagation is mainly supported by gap junctional coupling (see Section 3.1). When $0.7 \leqslant p \leqslant 0.9$, ephaptic coupling can thus reduce the number of CB, which points to an advantage of ephaptic coupling.

Recall from Sec. 3.2.3 that SAP occurs at $d_{\text{cleft}} = 3.5$ nm when $p = 1$. At $p = 0.9$ and $d_{\text{cleft}} = 3.5$ nm in Tables 2 and 3, SAP is seen when there is no CB.

3.3.2. Ephaptic coupling can enhance CB when $0.4 \leqslant p \leqslant 0.6$.

Tables 4 - 6 show the number of CB for different p and d_{cleft} in 6×75, 10×75 and 16×75 lattices, respectively. Note that CB was never observed in monogenotypic preparations ($p = 0$ or 1). Nevertheless, similarly to simulations discussed in the previous section, conduction is susceptible to CB in preparations with mixed WT and Cx43KO cells, especially for $0.4 \leqslant p \leqslant 0.6$. This is seen for all ephaptic coupling strengths and lattice widths.

It can be seen from Tables 2 - 6 that the number of CB generally decreases as the lattice becomes wider. This is most likely because the presence of a larger number of alternative pathways for propagation in wider lattices permits the wave-

front to bypass sites of low excitability. Exceptions to this rule are seen when $p = 0.9$, $d_{\text{cleft}} = 2$ nm and 3.5 nm. When $d_{\text{cleft}} = 2$ nm, the number of CB increases in wider lattices. When $d_{\text{cleft}} = 3.5$ nm, the number of CB displays an irregular dependency on the width of the lattice. The mechanism behind the phenomena is still unclear, but the unexplained variations are statistically significant.

The alleviatory effect of ephaptic coupling on CB in narrower lattices shown in Tables 2 and 3 (discussed in the previous section) is also present in wider lattices (Tables 4 - 6, $0.7 \leqslant p \leqslant 0.9$). The magnitude of this effect, seems to be smaller, however.

A new feature observed in wider lattices but not seen in narrower lattices is that the number of CB shows a dependency on d_{cleft} when $0.4 \leqslant p \leqslant 0.6$. As seen in Tables 4 - 6 the proportion of CB is *lower* at $d_{\text{cleft}} = 115$ nm than at smaller d_{cleft}. This implies that ephaptic coupling does not prevent, but rather, facilitates CB in this parameter range. Indeed, in Table 6, for $0.4 \leqslant p \leqslant 0.6$, the differences in the number of CB at $d_{\text{cleft}} = 115$ nm and smaller d_{cleft} are statistically significant according to the two-proportion z-test. Additionally, in Table 5, when $0.4 \leqslant p \leqslant 0.6$, the statistically significant differences in the occurrence of CB between $d_{\text{cleft}} = 115$ nm and $d_{\text{cleft}} = 8$ nm or 8.5 nm can be detected if 400 numerical experiments are performed (data is not shown in Table 5). In Table 4, for $p = 0.6$, a statistically significant difference between $d_{\text{cleft}} = 115$ nm and 8 nm can be seen if the number of numerical experiments is increased to 400 (data is not shown in Table 4). Ephaptic coupling can thus increase the possibility of CB in the co-cultures, which points to a disadvantage of ephaptic coupling. We see that this effect is more pronounced in wider lattices.

When $p = 0.9$, SAP still occurs at $d_{\text{cleft}} = 3.5$ nm in Tables 4 and 5, but the

number of occurrences of CB is 2 and 1, respectively.

We have checked that the effect of suppressing (Sec. 3.3.1) or promoting CB (Sec. 3.3.2) is only seen when Na^+ channels are localized to the cleft; indeed, when Na^+ channel is uniformly distributed, the number of CB is independent of d_{cleft} values and is almost the same as the numbers in Tables 2 - 6 for $d_{\text{cleft}} = 115$ nm (data is not shown). This implies that ephaptic coupling does not modulate CB when Na^+ channel distribution is uniform.

Table 2: Number of CB for a 2×75 lattice. For $0.7 \leqslant p \leqslant 0.8$, the differences in the number of CB at $d_{\text{cleft}} = 8$ nm and $d_{\text{cleft}} = 115$ nm are statistically significant according to the two-proportions z-test ($z = 3.6$ and 2.5, respectively). For $p = 0.9$, statistically significant difference ($z = 2.3$) can be detected if more than 800 numerical experiments are performed (data not shown).

d_{cleft} (nm) \ p	0	0.1	0.2	0.3	0.4	0.5	0.6	0.7	0.8	0.9	1
2	0	93	100	100	100	100	100	100	100	74	0
3.5	0	92	100	100	100	100	100	100	100	78	SAP
8	0	92	100	100	100	100	95	**55**	**16**	**3**	0
8.5	0	92	100	100	100	100	95	55	18	4	0
115	0	92	100	100	100	100	99	79	31	5	0

Table 3: Number of CB for a 3×75 lattice. For $p = 0.7$, according to the two-proportion z-test, we observed statistically significant difference ($z = 3.3$) in the occurrence of CB between $d_{\text{cleft}} = 8$ nm and 115 nm. At $p = 0.8$, statistically significant difference ($z = 4.8$) can be observed when the number of numerical experiments is increased to 400 (data not shown).

d_{cleft} (nm) \ p	0	0.1	0.2	0.3	0.4	0.5	0.6	0.7	0.8	0.9	1
2	0	48	99	100	100	100	100	100	100	80	0
3.5	0	35	94	100	100	100	100	100	100	83	SAP
8	0	35	93	100	100	100	98	**46**	**3**	0	0
8.5	0	35	93	100	100	100	97	51	5	0	0
115	0	35	94	100	100	100	99	69	10	1	0

Table 4: Number of CB for a 6×75 lattice, For $p = 0.6$, there are statistically significant differences in the occurrence of CB between $d_{\text{cleft}} = 115$ nm and $d_{\text{cleft}} = 2$ nm, 3.5 nm or 8 nm. In particular, the significant differences between $d_{\text{cleft}} = 115$ nm and $d_{\text{cleft}} = 8$ nm can be detected if 400 numerical experiments are performed (data not shown).

d_{cleft} (nm) \ p	0	0.1	0.2	0.3	0.4	0.5	0.6	0.7	0.8	0.9	1
2	0	15	97	100	100	100	**100**	100	100	79	0
3.5	0	0	25	91	100	100	**100**	100	98	93	SAP
8	0	0	24	88	100	100	**81**	23	1	0	0
8.5	0	0	24	88	100	99	74	14	0	0	0
115	0	0	24	87	99	100	**72**	18	2	0	0

Table 5: Number of CB for a 10×75 lattice. When $0.4 \leqslant p \leqslant 0.6$, there are statistically significant differences in the number of CB at $d_{\text{cleft}} = 115$ and smaller d_{cleft}. In particular, the statistically significant differences between $d_{\text{cleft}} = 115$ nm and $d_{\text{cleft}} = 8$ nm or 8.5 nm can be detected if 400 numerical experiments are performed (data not shown).

d_{cleft} (nm) \ p	0	0.1	0.2	0.3	0.4	0.5	0.6	0.7	0.8	0.9	1
2	0	4	89	100	**100**	**100**	**100**	100	100	92	0
3.5	0	0	3	74	**100**	**100**	**100**	100	52	54	SAP
8	0	0	1	41	**97**	**99**	**64**	0	0	0	0
8.5	0	0	1	40	**96**	**96**	**40**	0	0	0	0
115	0	0	1	39	**92**	**86**	**31**	0	0	0	0

Table 6: Number of CB for a 16×75 lattice. When $0.4 \leqslant p \leqslant 0.6$, the number of CB at $d_{\text{cleft}} = 115$ nm is significantly less than at smaller d_{cleft}.

d_{cleft} (nm) \ p	0	0.1	0.2	0.3	0.4	0.5	0.6	0.7	0.8	0.9	1
2	0	2	89	100	**100**	**100**	**100**	100	100	99	0
3.5	0	0	1	56	**100**	**100**	**100**	98	37	43	SAP
8	0	0	0	12	**83**	**99**	**50**	0	0	0	0
8.5	0	0	0	10	**79**	**97**	**27**	0	0	0	0
115	0	0	0	7	**59**	**53**	**8**	0	0	0	0

3.4. Mechanisms behind the increased proportions of CB.

As demonstrated in Sec. 3.3, a smaller d_{cleft} can either prevent or promote CB depending on parameter range. In wider lattices, CB is more frequent in the

presence of ephaptic coupling when $0.4 \leqslant p \leqslant 0.6$.

We now explore the mechanism behind this observation by using a representative example of 6×75 lattice at $p = 0.6$. A similar analysis can be performed in other cases as well. In Figs. 10 - 13, EAT is plotted at different iterations ($i = 9,\ 20,\ 35,\ 50$, respectively). In Figs. 10A, 11A, 12A, and 13A, $d_{\text{cleft}} = 2$ nm, 3.5 nm, 8 nm and 8.5 nm, respectively. In Figs. 10B, 11B, 12B and 13B, $d_{\text{cleft}} = 115$ nm. In each figure, panels A and B have the same distribution of Cx43 expression. We plotted EAT for instances in which CB is seen in the presence of ephaptic coupling ($d_{\text{cleft}} = 2$ nm, 3.5 nm, 8 nm, 8.5 nm) but not in its absence ($d_{\text{cleft}} = 115$ nm). At the location where CB is observed (denoted by EAT $= 0$) when ephaptic coupling is present (solid box in panel A), there is always a plateau phase of EAT when ephaptic coupling is absent (solid box in panel B). Similarly, when there is a gap in EAT in the presence of ephaptic coupling (dashed box in panel A), a plateau phase in the EAT is seen in its absence (dashed box in panel B). This implies the presence of relatively large cell clusters that are excited almost simultaneously when ephaptic coupling is absent, but are difficult or impossible to excite when ephaptic coupling is present.

In light of the foregoing, we may describe the mechanism as follows. For $0.4 \leqslant p \leqslant 0.6$, Cx43KO and WT cells are mixed in roughly equal proportion. The random distribution of cell genotypes results in local clusters of WT cells coupled through normal levels of gap junctions, which form electric loads that may substantially impair the conduction. When an action potential propagates into such cell clusters, the electric loads can lead to delayed activation or even CB if the activating current is not sufficiently strong.

In the presence of ephaptic coupling (at smaller d_{cleft}), R_c is high, and the cleft

potential may drop low enough to excite the end membrane of cell downstream, but the resulting inward current may not be sufficient to excite the entire cell. The high resistance creates a bottleneck that limits the amount of current into the cleft space and across the end membrane of neighboring cell. Ephaptic coupling may thus lead to a decrease in activating current for cells downstream, which together with the increased load discussed above (when $0.4 \leqslant p \leqslant 0.6$), may result in a prominent current-to-load mismatch.

4. Conclusions and Discussions

In this manuscript, we explored the interplay between reduced heterogeneous Cx43 expression and ephaptic coupling on cardiac action potential propagation. Under severely reduced Cx43 expression, we identified three new phenomena in the presence of ephaptic coupling: alternating conduction, in which ephaptic and gap junction-mediated mechanisms alternate; instability of planar fronts; and SAP which has a smaller potential amplitude than the normal action potential. We then examined the effects of heterogeneous Cx43 expression and ephaptic coupling on CB using a 2D cell lattice as our model system. We found that ephaptic coupling can either prevent or promote CB depending on the Cx43KO content. When Cx43KO content is relatively high ($0.7 \leqslant p \leqslant 0.9$), ephaptic coupling reduces the possibilities of CB, an effect that is greater in narrower lattices. In wider lattices, ephaptic coupling promotes CB when the Cx43KO content $0.4 \leqslant p \leqslant 0.6$. This increase in the probabilities of CB can be attributed to an increase in current-to-load mismatch.

We demonstrated the biphasic behavior of $\mathrm{CV_L}$ as a function of d_{cleft} when Cx43KO content is 100% (Sec. 3.1). This nonmonotonicity of $\mathrm{CV_L}$ qualitatively

agrees with previously published results shown in Kucera et al. (2002); Hand and Peskin (2010). In Kucera et al. (2002), the maximal CV_L (15 cm/s) under 1% of normal gap junction is achieved at $d_{cleft} = 40$ nm. In Hand and Peskin (2010), the maximal CV_L (20 cm/s) is obtained at $d_{cleft} = 11$ nm under 1% of normal gap junction expression. Although the optimal d_{cleft} values are quantitatively different from ours, the qualitative behavior of CV_L is similar.

This is the first study to examine the interaction between heterogeneous Cx43 expression and ephaptic coupling on the occurrence of CB (Sec. 3.3). CB, especially unidirectional CB (UCB) has been considered a substrate for fatal reentrant arrhythmias and sudden cardiac death Waldo and Wit (1993). Therefore, over the last decades, CB or UCB has become the major focus of research. We reported that ephaptic mechanism can lower the possibilities of CB when Cx43KO content $p \geqslant 0.7$, which implies an anti-arrhythmic role of ephaptic coupling when gap junctions are reduced. This finding is consistent with the result shown in Fig. 2A of Sec. 3.1 and earlier numerical (Mori et al. (2008); Hand and Peskin (2010); Lin and Keener (2014)) and experimental results (Yao et al. (2003); Veeraraghavan et al. (2012)), which suggested that ephaptic coupling can increase conduction speed when gap junction expression is low. On the other hand, we showed that ephaptic coupling can increase the proportion of CB when Cx43KO content $0.4 \leqslant p \leqslant 0.6$, which points to a disadvantageous role of ephaptic coupling in this context. This finding is also consistent with the result shown in Fig. 2B of Sec. 3.1, which suggests that ephaptic coupling can reduce conduction velocity when gap junctional coupling is sufficiently high. It is notable that similar results have been reported elsewhere in Kucera et al. (2002); Mori et al. (2008); Hand and Peskin (2010); Lin and Keener (2014). It is important to note, however, that previous

papers Yao et al. (2003); Mori et al. (2008); Hand and Peskin (2010); Veeraraghavan et al. (2012); Lin and Keener (2014) studied ephaptic coupling by examining its effect on conduction speed with a homogeneous change in gap junctional conductance. Our study focused on the reliability of cardiac signal propagation by studying CB in the presence of heterogeneous Cx43 expression.

Finally, we mention that all the effects of ephaptic coupling mentioned in our findings (results in Sec. 3) are shown to be highly dependent on the localized Na^+ channels, which are consistent with the experimental and numerical results in Cohen (1996); Maier et al. (2002); Kucera et al. (2002); Sperelakis and McConnell (2002); Hand and Peskin (2010); Veeraraghavan et al. (2014a); Lin and Keener (2014).

In this paper, we adopted a simplified geometry, cell discretization (each cell is treated to be isopotential) and arrangement of cells. We believe that using realistic cell shape or delicate cell arrangement (Prudat and Kucera (2014); Lin and Keener (2014)) will not qualitatively change our conclusions, but may lead to new phenomena. Although we identified some important features of conduction, alternating conduction, instability of planar fronts and SAP, the detailed mechanism behind these phenomena are still unclear. A future study with simplified models may allow us to obtain better understanding. Finally, we mention that the role of Cx43 may not be restricted to electrical conduction, as suggested in Lübkemeier et al. (2013). This is beyond the scope of our current paper, and is a subject for future study.

Author Contributions

N.W., Y.M. and E.G.T. designed research; N.W. performed the research; N.W., Y.M. and E.G.T. analyzed the data; and N.W., Y.M. and E.G.T. wrote the manuscript. All authors approved the final version of the paper.

Acknowledgement

This work was supported by National Science Foundation [DMS 1516978 to Y.M. and PHY 1255410 and CMMI 1233951 to E.G.T.].

505 ## 5. References

506 Beauchamp, P., Choby, C., Desplantez, T., de Peyer, K., Green, K., Yamada, K. A.,
507 Weingart, R., Saffitz, J. E., Kléber, A. G., 2004. Electrical propagation in syn-
508 thetic ventricular myocyte strands from germline connexin43 knockout mice.
509 Circ. Res. 95 (2), 170–178.

510 Beauchamp, P., Desplantez, T., McCain, M. L., Li, W., Asimaki, A., Rigoli, G.,
511 Parker, K. K., Saffitz, J. E., Kleber, A. G., 2012. Electrical coupling and propa-
512 gation in engineered ventricular myocardium with heterogeneous expression of
513 connexin43. Circ. Res. 110 (11), 1445–1453.

514 Cohen, S. A., 1996. Immunocytochemical localization of rh1 sodium channel in
515 adult rat heart atria and ventricle presence in terminal intercalated disks. Circu-
516 lation 94 (12), 3083–3086.

517 Copene, E. D., Keener, J. P., 2008. Ephaptic coupling of cardiac cells through the
518 junctional electric potential. J. Math. Biol. 57 (2), 265–284.

519 Danik, S. B., Liu, F., Zhang, J., Suk, H. J., Morley, G. E., Fishman, G. I., Gutstein,
520 D. E., 2004. Modulation of cardiac gap junction expression and arrhythmic
521 susceptibility. Circ. Res. 95 (10), 1035–1041.

522 Davis, L. M., Rodefeld, M. E., Green, K., Beyer, E. C., Saffitz, J. E., 1995. Gap
523 junction protein phenotypes of the human heart and conduction system. J. Car-
524 diovasc. Electrophysiol. 6 (10), 813–822.

525 Gutstein, D. E., Morley, G. E., Vaidya, D., Liu, F., Chen, F. L., Stuhlmann, H.,
526 Fishman, G. I., 2001. Heterogeneous expression of gap junction channels in

527 the heart leads to conduction defects and ventricular dysfunction. Circulation
528 104 (10), 1194–1199.

529 Hand, P. E., Griffith, B. E., Peskin, C. S., 2009. Deriving macroscopic myocar-
530 dial conductivities by homogenization of microscopic models. Bull. Math. Biol.
531 71 (7), 1707–1726.

532 Hand, P. E., Peskin, C. S., 2010. Homogenization of an electrophysiological
533 model for a strand of cardiac myocytes with gap-junctional and electric-field
534 coupling. Bull. Math. Biol. 72 (6), 1408–1424.

535 HUANG, X.-D., Sandusky, G. E., ZIPES, D. P., 1999. Heterogeneous loss of con-
536 nexin43 protein in ischemic dog hearts. J. Cardiovasc. Electrophysiol. 10 (1),
537 79–91.

538 Iida, M., Lui, R., Ninomiya, H., 2011. Stacked fronts for cooperative systems with
539 equal diffusion coefficients. Siam J. Math. Anal. 43 (3), 1369–1389.

540 Jongsma, H. J., Wilders, R., 2000. Gap junctions in cardiovascular disease. Circ.
541 Res. 86 (12), 1193–1197.

542 Kanno, S., Saffitz, J. E., 2001. The role of myocardial gap junctions in electrical
543 conduction and arrhythmogenesis. Cardiovasc. Pathol. 10 (4), 169–177.

544 Keener, J., Sneyd, J., 2010. Mathematical physiology: I: cellular physiology.
545 Vol. 1. Springer Science & Business Media.

546 Kucera, J. P., Rohr, S., Rudy, Y., 2002. Localization of sodium channels in inter-
547 calated disks modulates cardiac conduction. Circ. Res 91 (12), 1176–1182.

548 Lin, J., Keener, J. P., 2014. Microdomain effects on transverse cardiac propaga-
549 tion. Biophys. J. 106 (4), 925–931.

550 Livshitz, L. M., Rudy, Y., 2007. Regulation of ca2+ and electrical alternans in
551 cardiac myocytes: role of camkii and repolarizing currents. Am. J. Physiol.
552 Heart Circ. Physiol. 292 (6), H2854–H2866.

553 Lübkemeier, I., Requardt, R. P., Lin, X., Sasse, P., Andrié, R., Schrickel, J. W.,
554 Chkourko, H., Bukauskas, F. F., Kim, J.-S., Frank, M., et al., 2013. Deletion of
555 the last five c-terminal amino acid residues of connexin43 leads to lethal ven-
556 tricular arrhythmias in mice without affecting coupling via gap junction chan-
557 nels. Basic Res. Cardiol. 108 (3), 1–16.

558 Maier, S. K., Westenbroek, R. E., Schenkman, K. A., Feigl, E. O., Scheuer, T.,
559 Catterall, W. A., 2002. An unexpected role for brain-type sodium channels in
560 coupling of cell surface depolarization to contraction in the heart. Proc. Natl.
561 Acad. Sci. 99 (6), 4073–4078.

562 McCain, M. L., Desplantez, T., Geisse, N. A., Rothen-Rutishauser, B., Oberer,
563 H., Parker, K. K., Kleber, A. G., 2012. Cell-to-cell coupling in engineered pairs
564 of rat ventricular cardiomyocytes: relation between cx43 immunofluorescence
565 and intercellular electrical conductance. Am. J. Physiol. Heart Circ. Physiol.
566 302 (2), H443–H450.

567 Mori, Y., Fishman, G. I., Peskin, C. S., 2008. Ephaptic conduction in a cardiac
568 strand model with 3d electrodiffusion. Proc. Natl. Acad. Sci. 105 (17), 6463–
569 6468.

570 Mori, Y., Matano, H., 2015. Stability of front solutions of the bidomain equation.
571 Comm. Pure Appl. Math. In press.

572 Prudat, Y., Kucera, J. P., 2014. Nonlinear behaviour of conduction and block in
573 cardiac tissue with heterogeneous expression of connexin 43. J. Mol. Cell. Car-
574 diol. 76, 46–54.

575 Rohr, S., 2004. Role of gap junctions in the propagation of the cardiac action
576 potential. Cardiovasc. Res. 62 (2), 309–322.

577 Rohr, S., Kucera, J. P., Kléber, A. G., 1998. Slow conduction in cardiac tissue, i
578 effects of a reduction of excitability versus a reduction of electrical coupling on
579 microconduction. Circ. Res. 83 (8), 781–794.

580 Shaw, R. M., Rudy, Y., 1997. Ionic mechanisms of propagation in cardiac tissue
581 roles of the sodium and l-type calcium currents during reduced excitability and
582 decreased gap junction coupling. Circ. Res. 81 (5), 727–741.

583 Sperelakis, N., Mann, J. E., 1977. Evaluation of electric field changes in the cleft
584 between excitable cells. J. Theor. Biol 64 (1), 71–96.

585 Sperelakis, N., McConnell, K., 2002. Electric field interactions between closely
586 abutting excitable cells. IEEE Eng. Med. Biol. 21 (1), 77–89.

587 Vaidya, D., Tamaddon, H. S., Lo, C. W., Taffet, S. M., Delmar, M., Morley, G. E.,
588 Jalife, J., 2001. Null mutation of connexin43 causes slow propagation of ven-
589 tricular activation in the late stages of mouse embryonic development. Circ.
590 Res. 88 (11), 1196–1202.

591 Veeraraghavan, R., Lin, J., Hoeker, G. S., Keener, J. P., Gourdie, R. G., Poelzing,
592 S., 2014a. Sodium channels in the cx43 gap junction perinexus may constitute
593 a cardiac ephapse: an experimental and modeling study. Pflügers Arch.-Eur. J.
594 Physiol., 1–13.

595 Veeraraghavan, R., Poelzing, S., Gourdie, R. G., 2014b. Intercellular electrical
596 communication in the heart: a new, active role for the intercalated disk. Cell
597 communication & adhesion 21 (3), 161–167.

598 Veeraraghavan, R., Salama, M. E., Poelzing, S., 2012. Interstitial volume modu-
599 lates the conduction velocity-gap junction relationship. Am. J. Physiol. Heart
600 Circ. Physiol. 302 (1), H278–H286.

601 Waldo, A., Wit, A., 1993. Mechanisms of cardiac arrhythmias. The Lancet
602 341 (8854), 1189–1193.

603 Wang, X., Gerdes, A. M., 1999. Chronic pressure overload cardiac hypertrophy
604 and failure in guinea pigs: Iii. intercalated disc remodeling. J. Mol. Cell. Car-
605 diol. 31 (2), 333–343.

606 Yao, J.-A., Gutstein, D. E., Liu, F., Fishman, G. I., Wit, A. L., 2003. Cell coupling
607 between ventricular myocyte pairs from connexin43-deficient murine hearts.
608 Circ. Res. 93 (8), 736–743.

609 Yoshida, M., Ohkusa, T., Nakashima, T., Takanari, H., Yano, M., Takemura, G.,
610 Honjo, H., Kodama, I., Mizukami, Y., Matsuzaki, M., 2011. Alterations in ad-
611 hesion junction precede gap junction remodelling during the development of
612 heart failure in cardiomyopathic hamsters. Cardiovasc. Res. 92 (1), 95–105.

6. Figure captions

Fig. 1: A lattice view of a 2D bidomain model in the presence of ephaptic coupling (A) and circuit diagram for two adjacent cells coupled through a shared cleft in the presence of end-to-end gap junctions (GJ_{end}) (B), side-to-side gap junctions (GJ_{side}) and resistive connections between extracellular spaces (R_{ee}) are not shown here. This diagram is not to scale, as the cleft width is three orders of magnitude smaller than the length of cell. $\phi_i^{(i,j)}$ and $\phi_i^{(i,j+1)}$ represent intracellular potentials of cells at location (i,j) and $(i,j+1)$, respectively. $\phi_e^{(i,j)}$ and $\phi_e^{(i,j+1)}$ represent extracellular potentials of cells (i,j) and $(i,j+1)$, respectively. Cleft space was modelled as a narrow compartment between cells (i,j) and $(i,j+1)$, which is resistively connected (R_c) to the extracellular space. Cleft potential $\phi_c^{(i,j+\frac{1}{2})}$ is defined at location $(i,j+\frac{1}{2})$. The space, which lies in the extracellular space and stays adjacent to the aforementioned cleft is called the extracellular-cleft space. The potential in the extracellular-cleft space is denoted by $\phi_{ec}^{(i,j+\frac{1}{2})}$. Resistive connections between extracellular space and the extracellular-cleft space are denoted by R_{ec}.

Fig. 2: CV_{L} as a function of d_{cleft} for $p=1$ (A, Cx43KO) and $p=0$ (B, WT).

Fig. 3: EAT as a function of N at $d_{\text{cleft}} = 8.5$ nm (A), 8.6 nm (B), 8.7 nm (C), 8.9 nm (D).

Fig. 4: End transmembrane potential ($\phi_{ic} = \phi_i - \phi_c$) traces of the left ($\phi_{ic\text{L}}$) and right ($\phi_{ic\text{R}}$) sides of cells at location (3, 24), (3, 25), (3, 26) and (3, 27), where $d_{\text{cleft}} = 5$ nm (A), 8.9 nm (B) and 10 nm (C).

Fig. 5: Instability of planar fronts. A sequence of snapshots of propagation, illustrating ϕ at $t = 89$ ms (A), 112 ms (B), 139 ms (C) and 173 ms (D), respectively at $d_{\text{cleft}} = 9.8$ nm.

Fig. 6: SAP. A sequence of snapshots illustrate ϕ at $t = 13$ ms (A), 51 ms (B), 80 ms (C) and 126 ms (D), respectively for $d_{\text{cleft}} = 3.5$ nm.

Fig. 7: Intermediate wave. A sequence of snapshots illustrate ϕ at $t = 13$ ms (A), 54 ms (B), 77 ms (C) and 107 ms (D), respectively for $d_{\text{cleft}} = 3.8$ nm.

Fig. 8: Activation gating variable (m) profile of Na^+ channels residing on the end membrane (A) and ϕ profile (B) of cell (3, 25) at $d_{\text{cleft}} = 3.5$ nm.

Fig. 9: Activation gating variable (d) profile of L-type Ca^{2+} channels residing on the end (A), side (B) membranes and ϕ profile (C) of cell (3, 25), where $d_{\text{cleft}} =$ 3.5 nm (blue), 3.8 nm (red), and 115 nm (green).

Fig. 10: Representative plots of EAT along a 6×75 lattice at the 9^{th} iteration, where $p = 0.6$, $d_{\text{cleft}} = 2$ nm (A), 115 nm (B). Conduction delays and CB (A) are denoted by dashed and solid boxes, respectively. Plateau phase of EAT (B) corresponding to conduction delays and CB are denoted by dash and solid boxes, respectively.

Fig. 11: Representative plots of EAT along a 6×75 lattice at the 20^{th} iteration, where $p = 0.6$, $d_{\text{cleft}} = 3.5$ nm (A), 115 nm (B). Conduction delays and CB (A) are denoted by dashed and solid boxes, respectively. Plateau phase of EAT (B) corresponding to conduction delays and CB are denoted by dash and solid boxes, respectively.

Fig. 12: Representative plots of EAT along a 6×75 lattice at the 35^{th} iteration, where $p = 0.6$, $d_{\text{cleft}} = 8$ nm (A), 115 nm (B). Conduction delays and CB (A) are denoted by dashed and solid boxes, respectively. Plateau phase of EAT (B) corresponding to conduction delays and CB are denoted by dash and solid boxes, respectively.

Fig. 13: Representative plots of EAT along a 6×75 lattice at the 50^{th} iteration,

where $p = 0.6$, $d_{\text{cleft}} = 8.5$ nm (A), 115 nm (B). Conduction delays and CB (A) are denoted by dashed and solid boxes, respectively. Plateau phase of EAT (B) corresponding to conduction delays and CB are denoted by dash and solid boxes, respectively.

667 # 7. Figures

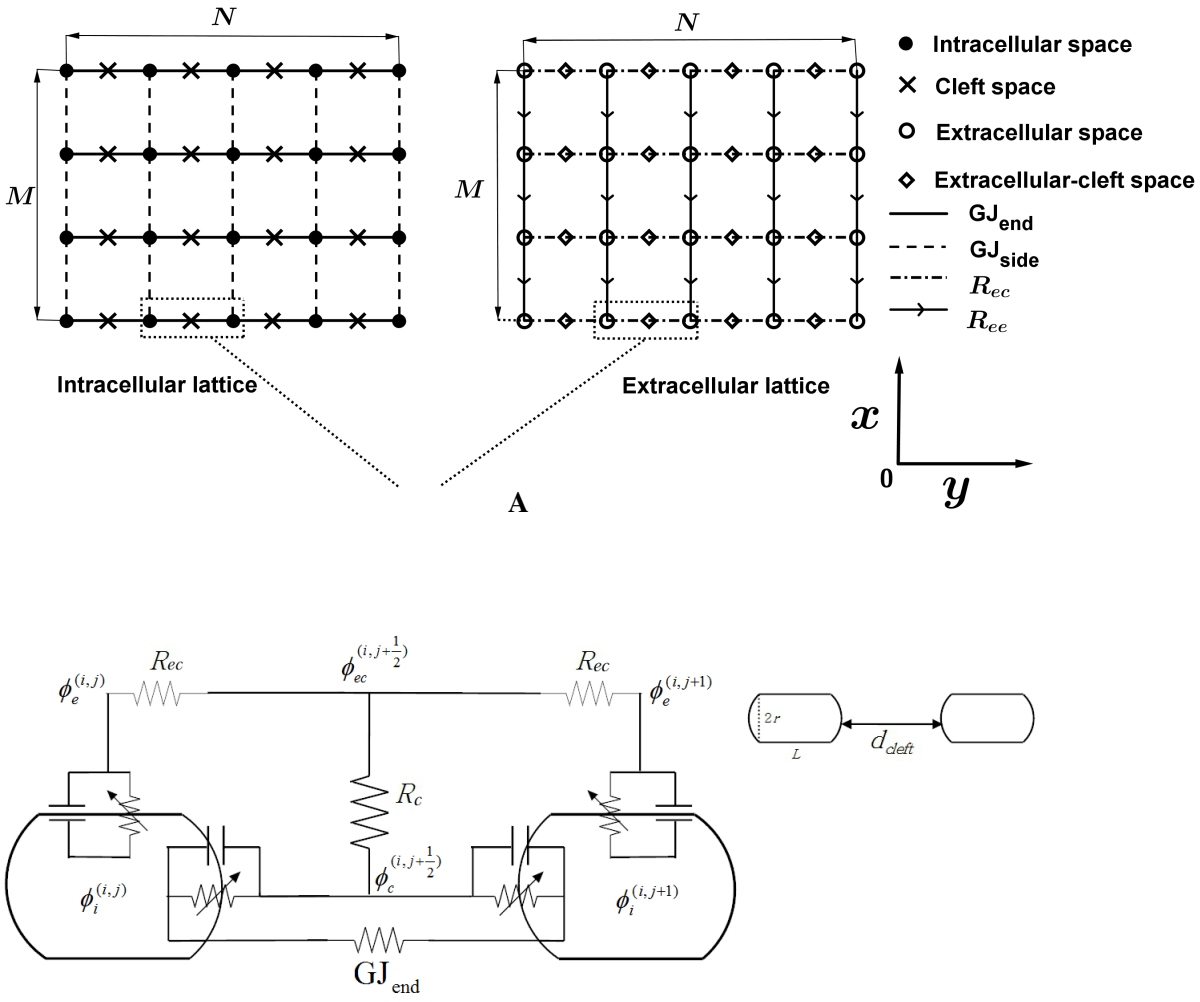

Figure 1

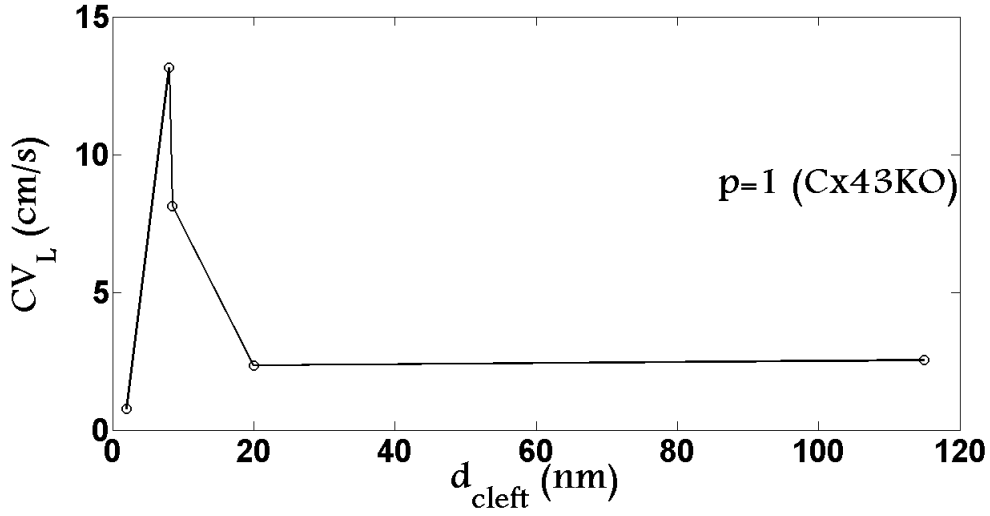
15
10
5
0
0
20
40
60
80
100
120
CV_L (cm/s)
d_cleft (nm)
p=1 (Cx43KO)

A

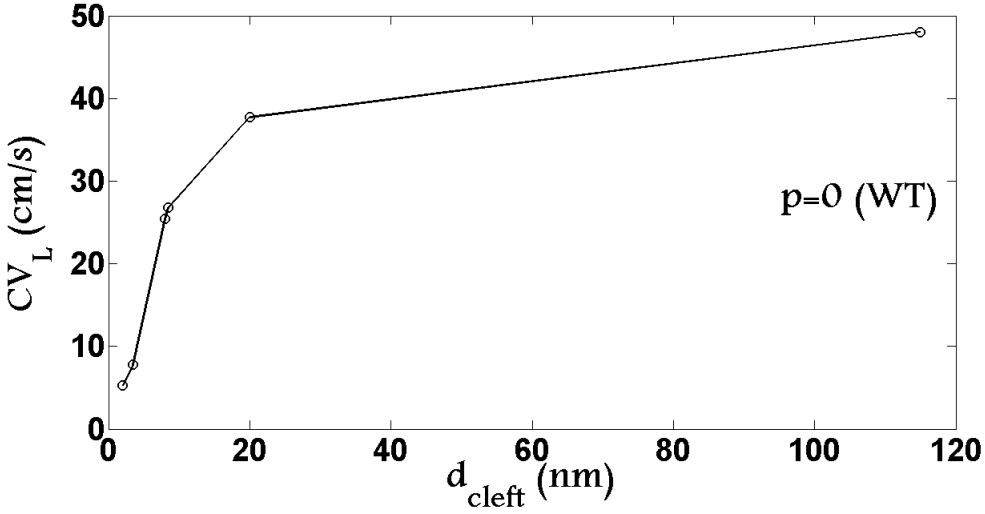
50
40
30
20
10
0
0
20
40
60
80
100
120
CV_L (cm/s)
d_cleft (nm)
p=0 (WT)

B

Figure 2

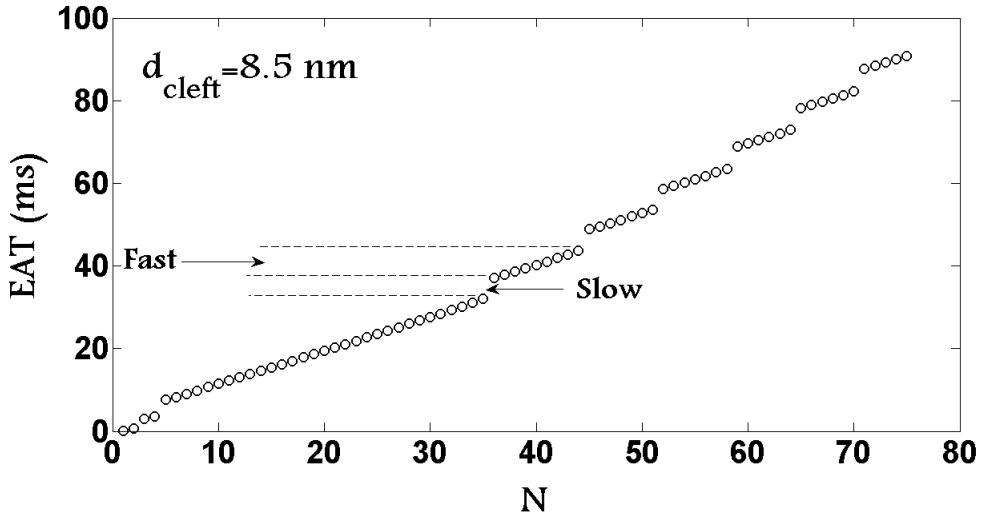
d cleft=8.5 nm
EAT (ms)
N
Fast
Slow
0
20
40
60
80
100
0
10
20
30
40
50
60
70
80

A

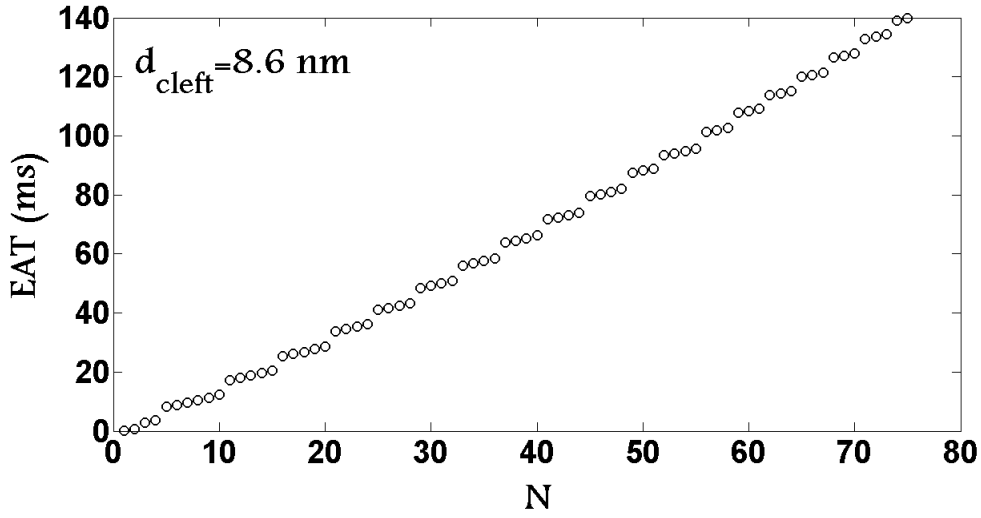
d cleft=8.6 nm
EAT (ms)
N
0
20
40
60
80
100
120
140
0
10
20
30
40
50
60
70
80

B

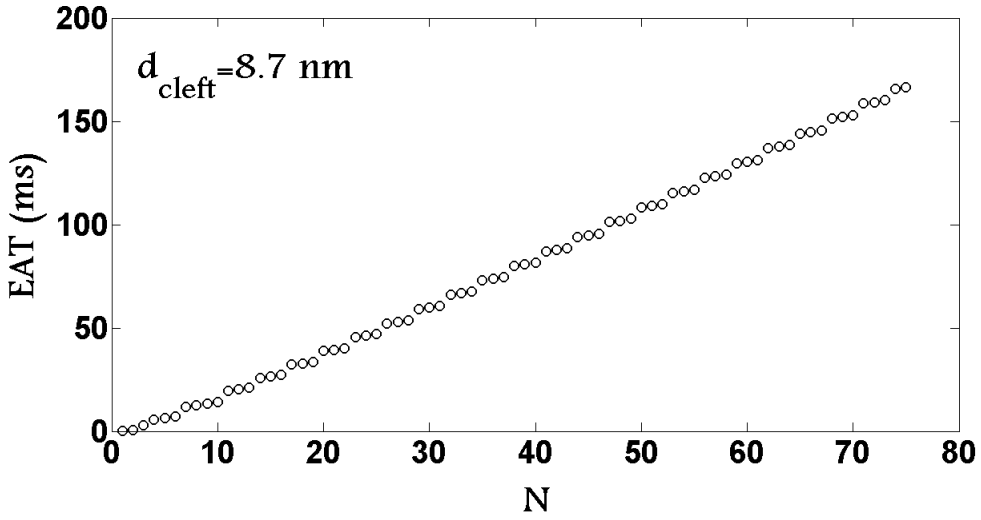
d cleft=8.7 nm
EAT (ms)
N
0
50
100
150
200
0
10
20
30
40
50
60
70
80

C

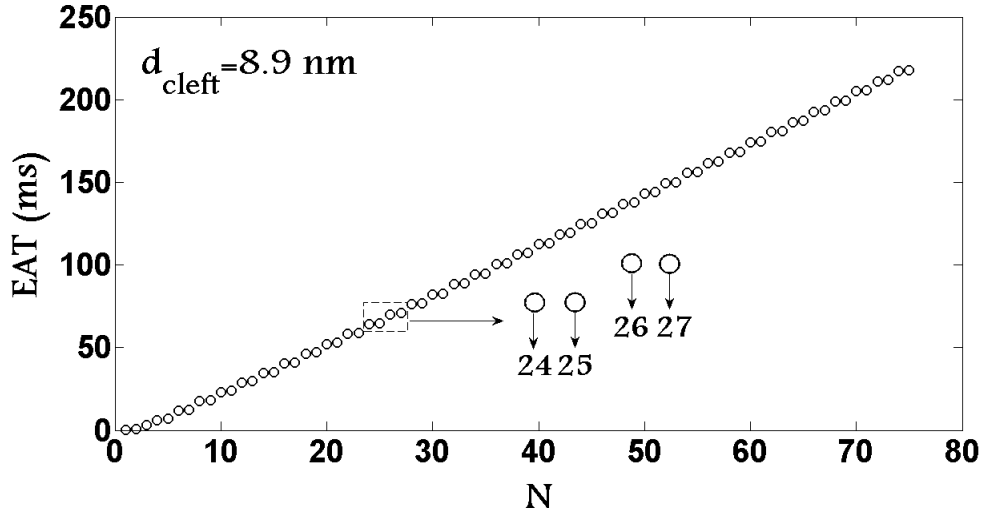
d cleft=8.9 nm
EAT (ms)
N
24 25
26 27
0
50
100
150
200
250
0
10
20
30
40
50
60
70
80

D

Figure 3

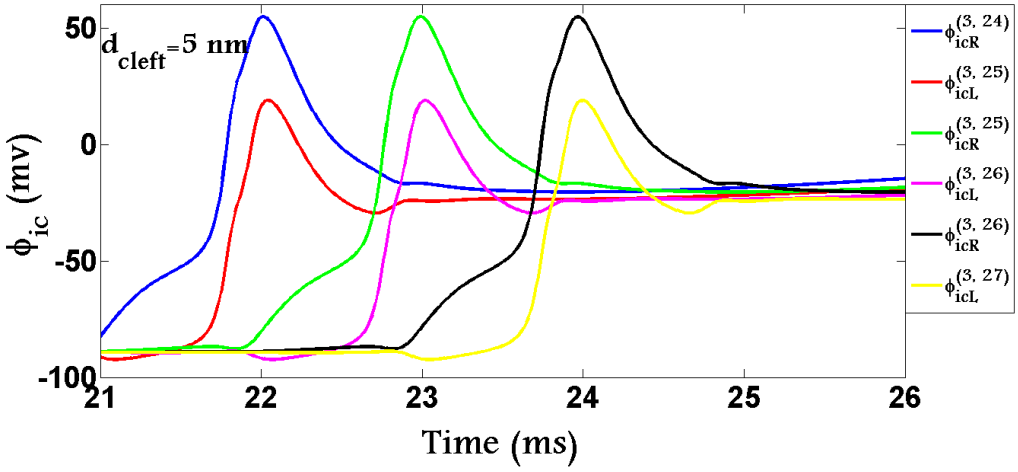
d cleft=5 nm
ϕ ic (mv)
Time (ms)
50
0
-50
-100
21
22
23
24
25
26
ϕ(3, 24) icR
ϕ(3, 25) icL
ϕ(3, 25) icR
ϕ(3, 26) icL
ϕ(3, 26) icR
ϕ(3, 27) icL

A

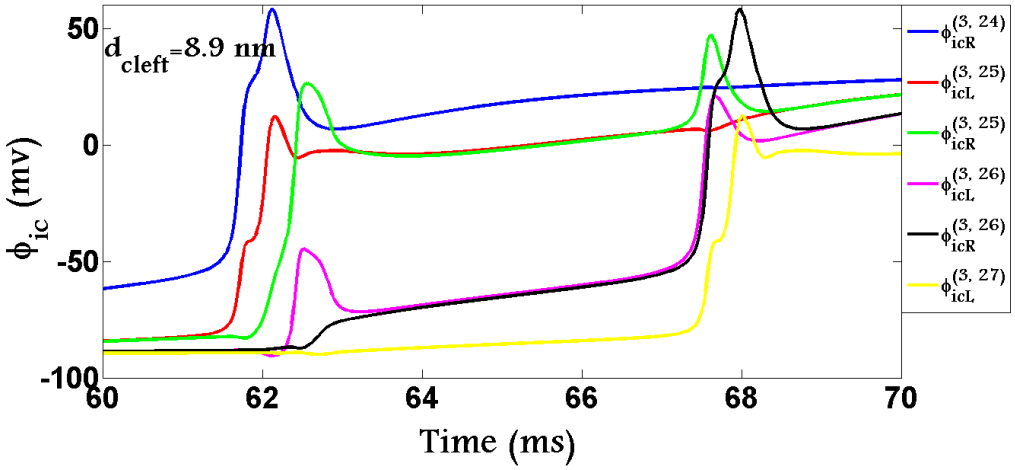
d cleft=8.9 nm
ϕ ic (mv)
Time (ms)
50
0
-50
-100
60
62
64
66
68
70
ϕ(3, 24) icR
ϕ(3, 25) icL
ϕ(3, 25) icR
ϕ(3, 26) icL
ϕ(3, 26) icR
ϕ(3, 27) icL

B

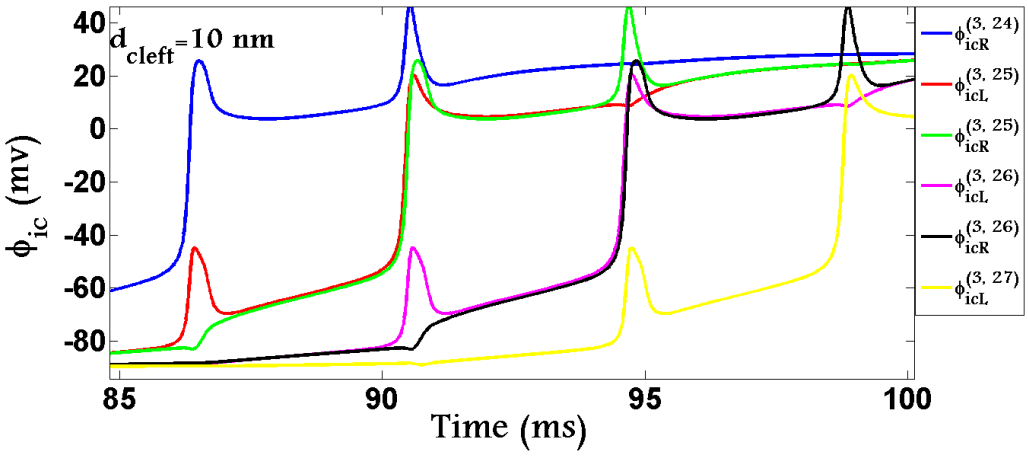
d cleft=10 nm
ϕ ic (mv)
Time (ms)
40
20
0
-20
-40
-60
-80
85
90
95
100
ϕ(3, 24) icR
ϕ(3, 25) icL
ϕ(3, 25) icR
ϕ(3, 26) icL
ϕ(3, 26) icR
ϕ(3, 27) icL

C

Figure 4

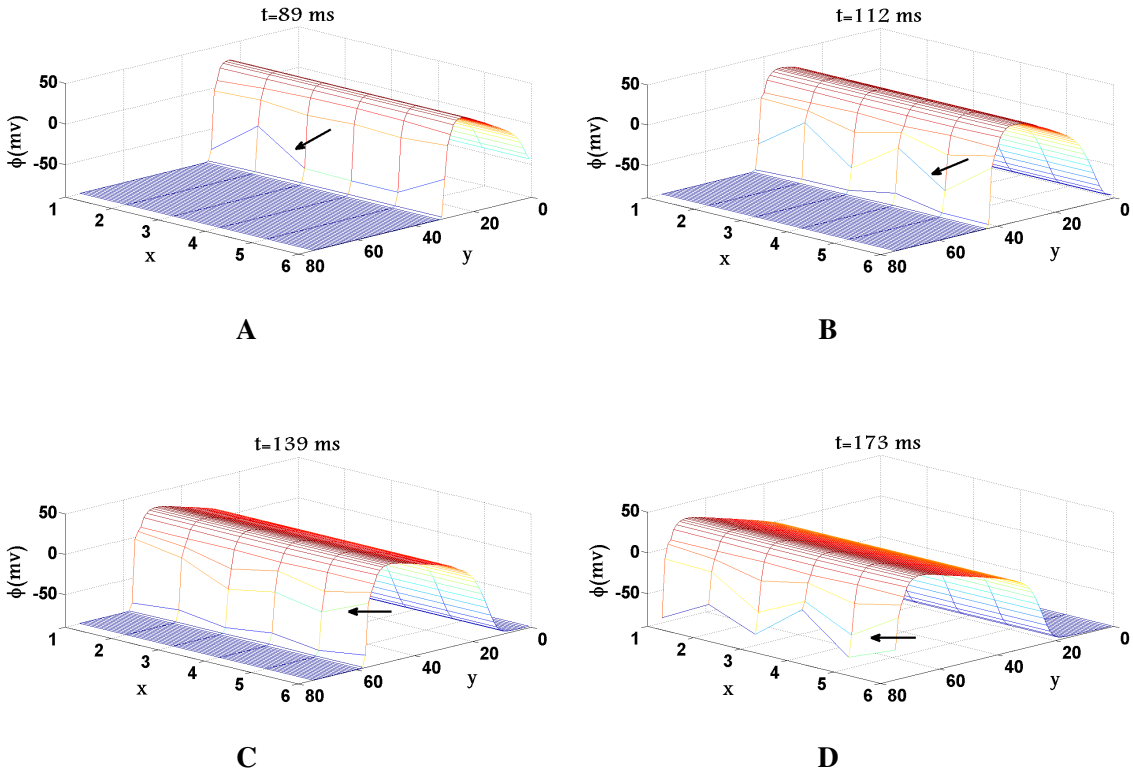
t=89 ms
t=112 ms
t=139 ms
t=173 ms
ϕ(mv)
50
0
-50
x
y
1
2
3
4
5
6
80
60
40
20
0
A
B
C
D

Figure 5

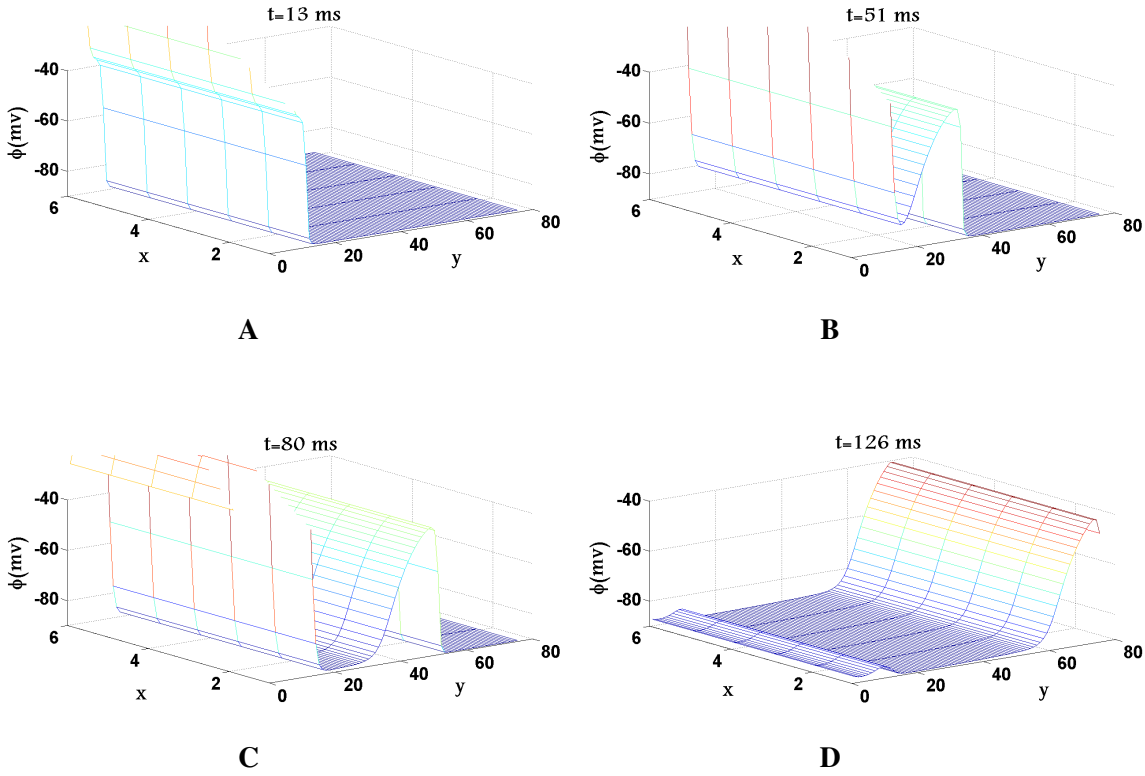

Figure 6

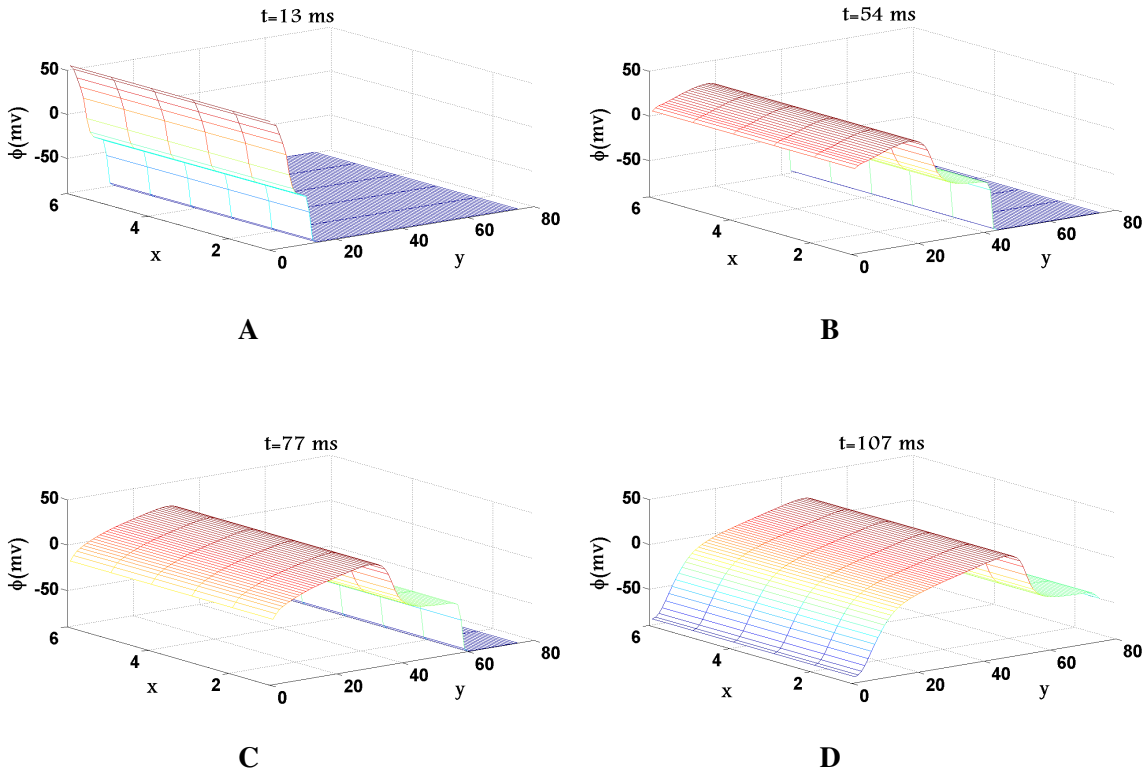

Figure 7

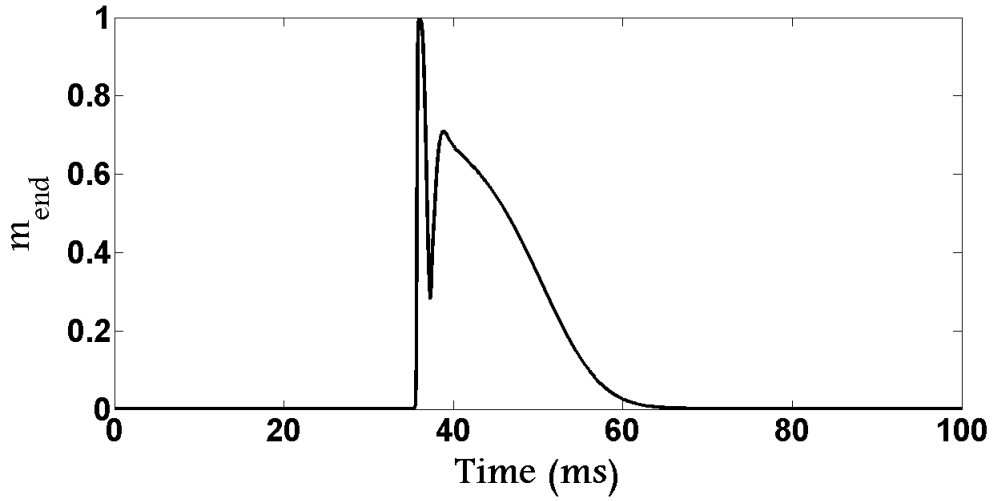
1
0.8
0.6
0.4
0.2
0
m end
0
20
40
60
80
100
Time (ms)

A

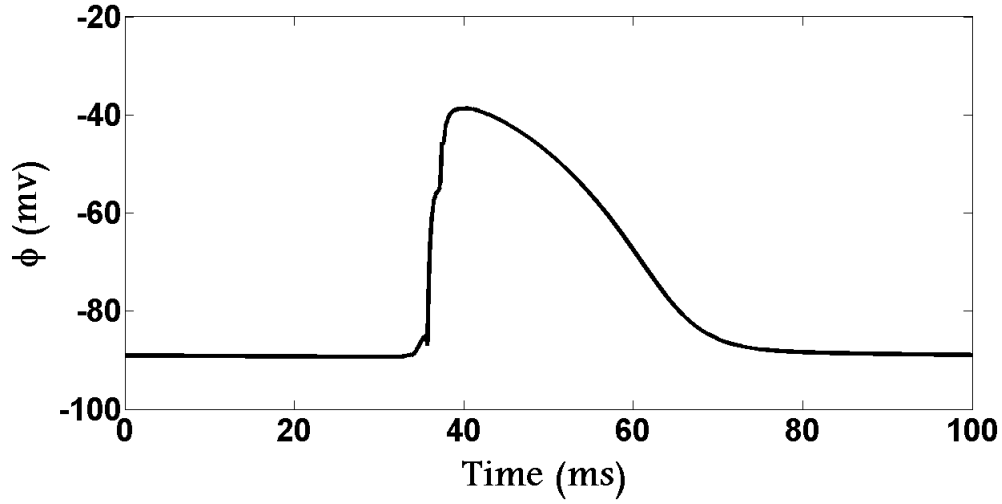
-20
-40
-60
-80
-100
ϕ (mv)
0
20
40
60
80
100
Time (ms)

B

Figure 8

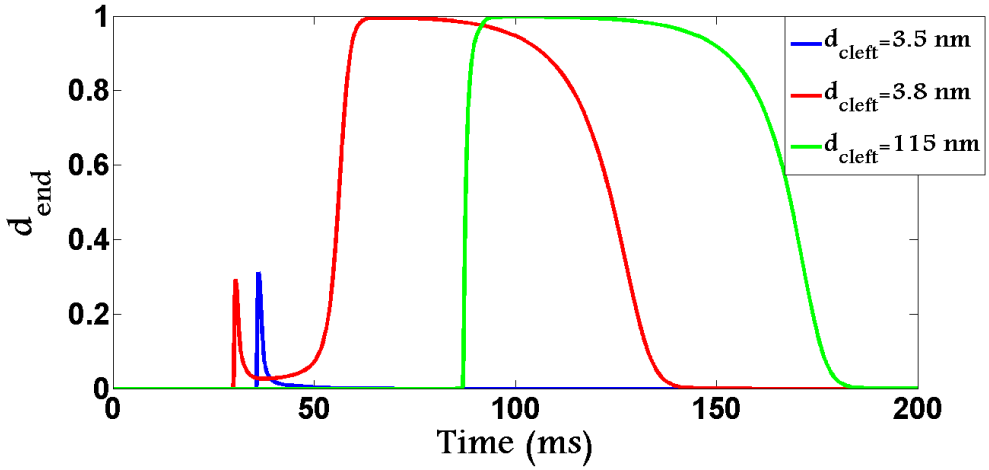
1
0.8
0.6
0.4
0.2
0
d end
0
50
100
150
200
Time (ms)
d cleft=3.5 nm
d cleft=3.8 nm
d cleft=115 nm

A

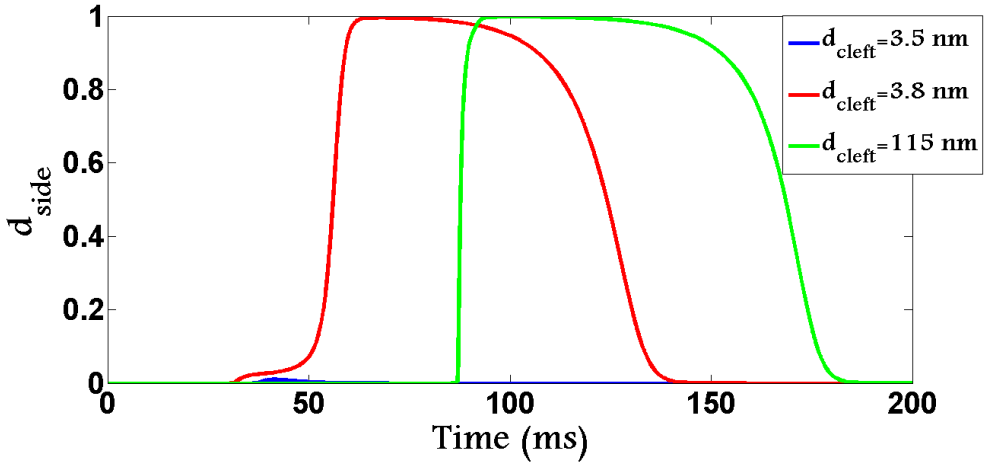
1
0.8
0.6
0.4
0.2
0
d side
0
50
100
150
200
Time (ms)
d cleft=3.5 nm
d cleft=3.8 nm
d cleft=115 nm

B

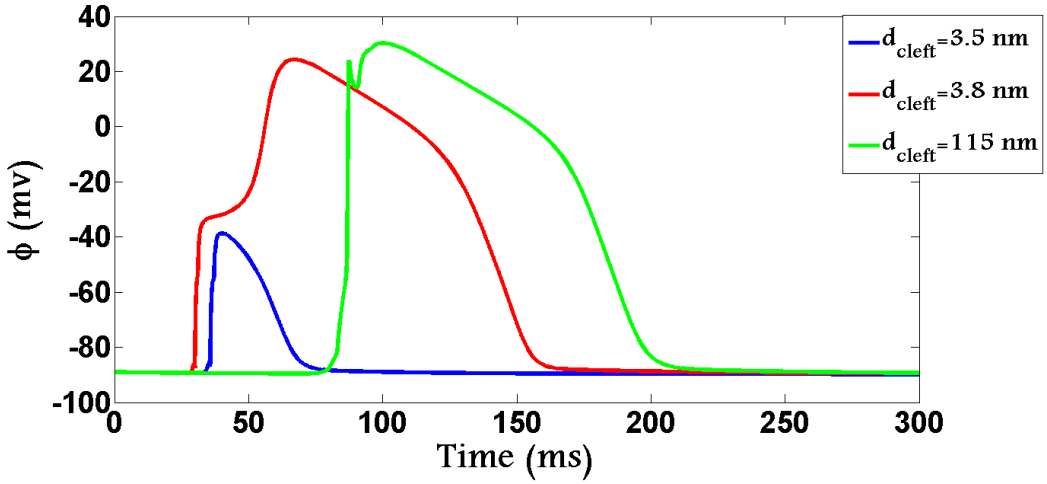
40
20
0
-20
-40
-60
-80
-100
ϕ (mv)
0
50
100
150
200
250
300
Time (ms)
d cleft=3.5 nm
d cleft=3.8 nm
d cleft=115 nm

C

Figure 9

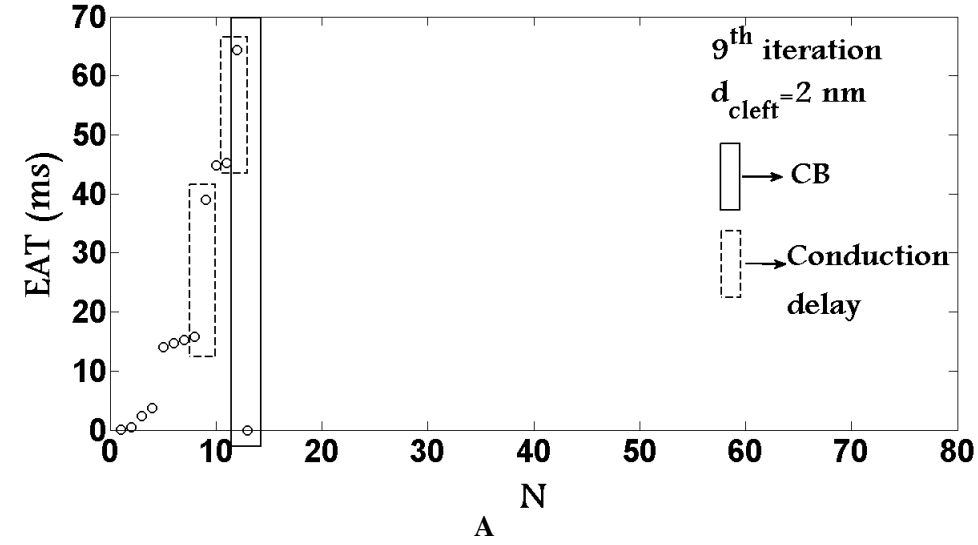
EAT (ms)
N
9th iteration
dcleft=2 nm
CB
Conduction
delay

A

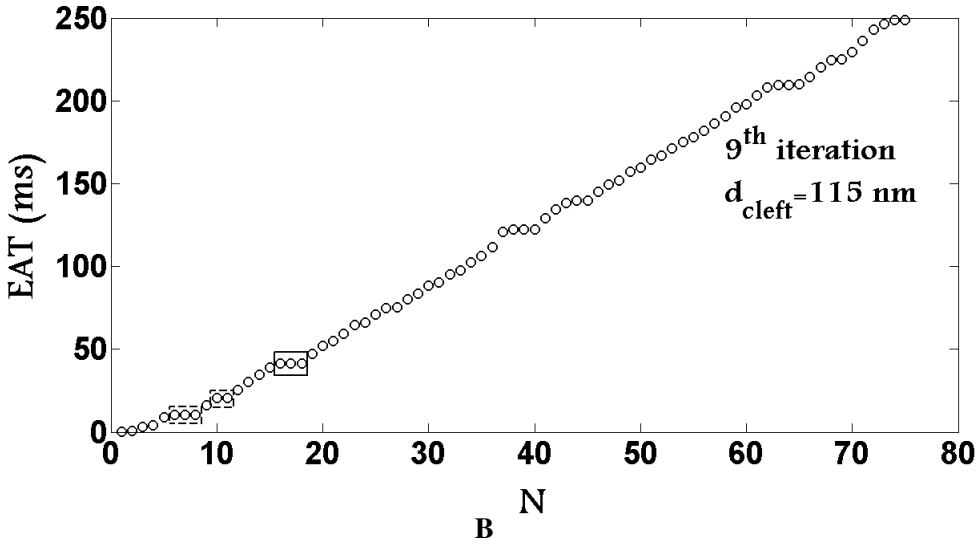
EAT (ms)
N
9th iteration
dcleft=115 nm

B

Figure 10

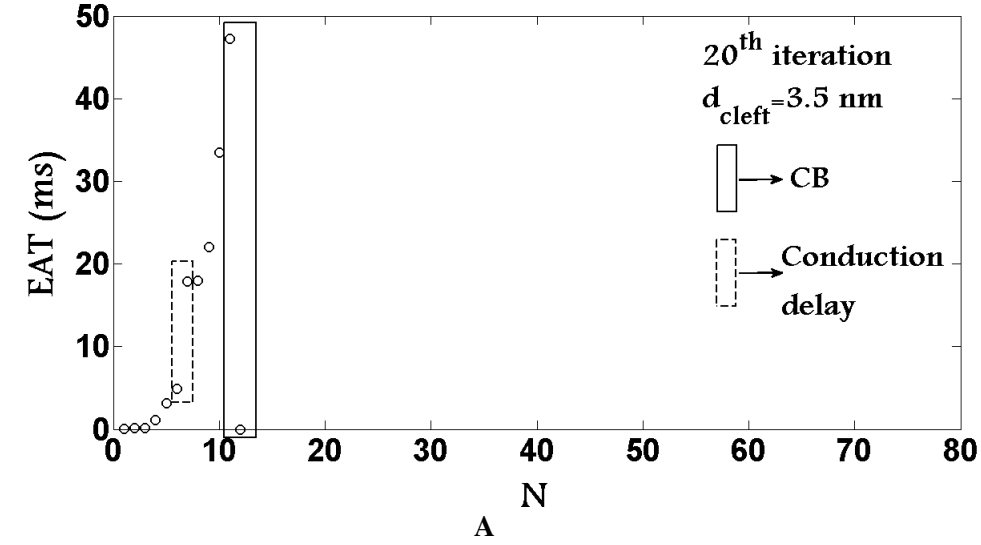
EAT (ms)
N
20th iteration
dcleft=3.5 nm
CB
Conduction
delay

A

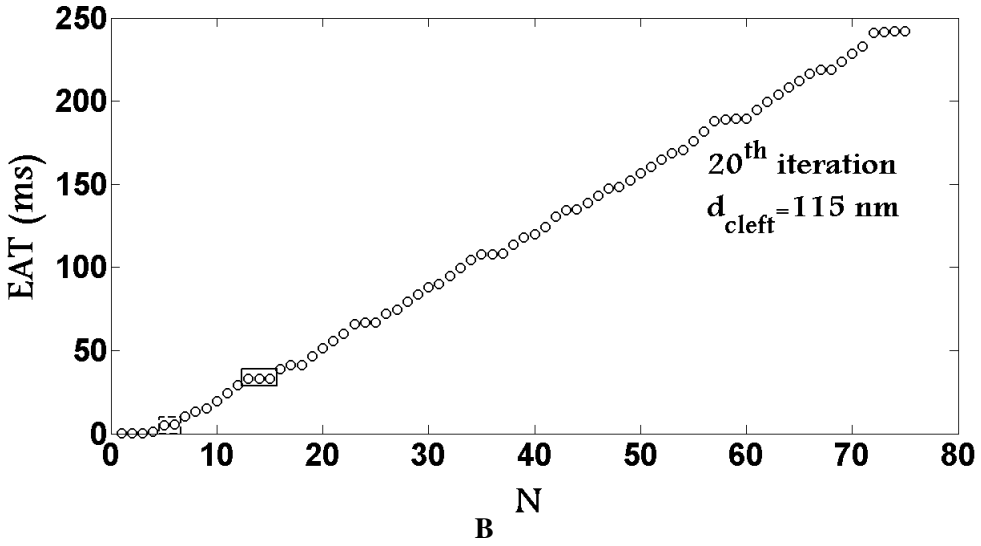
EAT (ms)
N
20th iteration
dcleft=115 nm

B

Figure 11

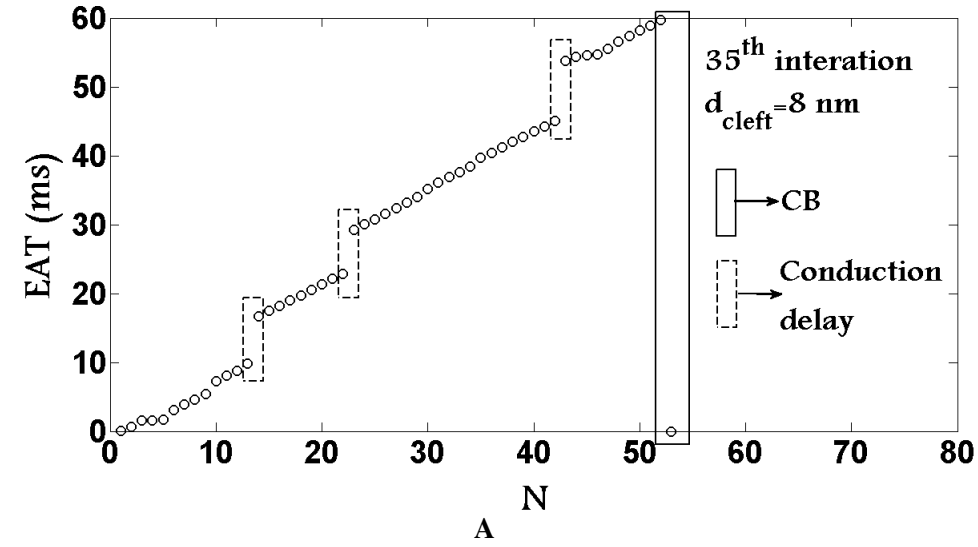
60
50
40
30
20
10
0
EAT (ms)
0
10
20
30
40
50
60
70
80
N
35th interation
dcleft=8 nm
CB
Conduction
delay

A

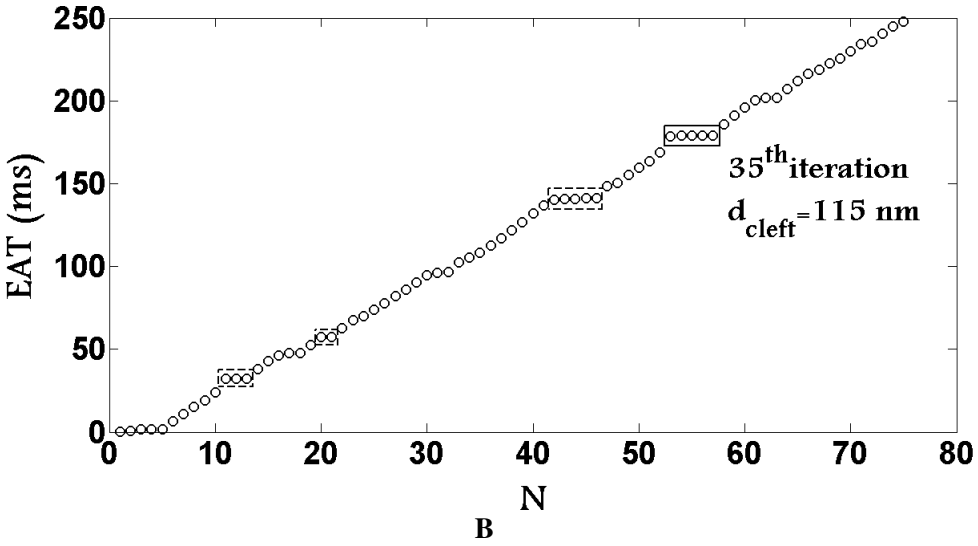
250
200
150
100
50
0
EAT (ms)
0
10
20
30
40
50
60
70
80
N
35thiteration
dcleft=115 nm

B

Figure 12

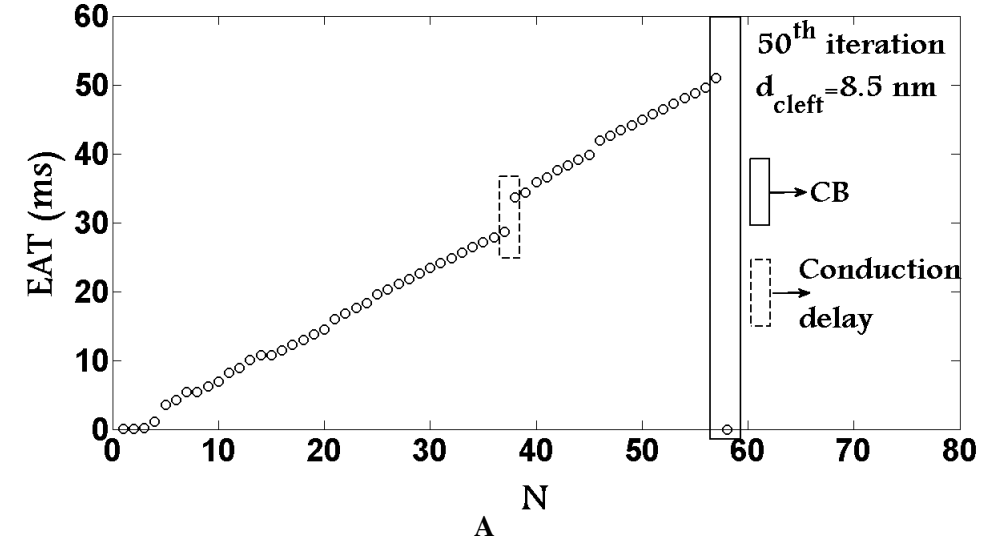
60
50
40
30
20
10
0
EAT (ms)
0
10
20
30
40
50
60
70
80
N
50th iteration
dcleft=8.5 nm
CB
Conduction
delay

A

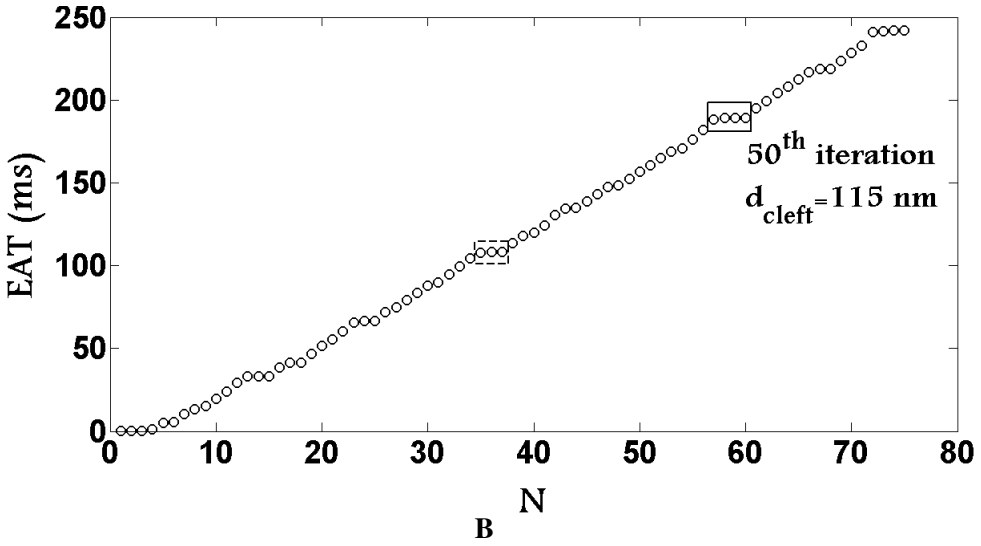
250
200
150
100
50
0
EAT (ms)
0
10
20
30
40
50
60
70
80
N
50th iteration
dcleft=115 nm

B

Figure 13